ARMY RESEARCH LABORATORY

Control Performance, Aerodynamic Modeling, and Validation of Coupled Simulation Techniques for Guided Projectile Roll Dynamics

by Jubaraj Sahu, Frank Fresconi, and Karen R. Heavey

ARL-TR-6997 **November 2014**

NOTICES

Disclaimers

Army Research Laboratory
Aberdeen Proving Ground, MD 21005-5069

ARL-TR-6997 **November 2014**

Control Performance, Aerodynamic Modeling, and Validation of Coupled Simulation Techniques for Guided Projectile Roll Dynamics

Jubaraj Sahu, Frank Fresconi, and Karen R. Heavey
Weapons and Materials Research Directorate, ARL

REPORT DOCUMENTATION PAGE			*Form Approved* *OMB No. 0704-0188*

1. REPORT DATE *(DD-MM-YYYY)*	November 2014
2. REPORT TYPE	Final
3. DATES COVERED (From - To)	January 2013–May 2014
4. TITLE AND SUBTITLE	Control Performance, Aerodynamic Modeling, and Validation of Coupled Simulation Techniques for Guided Projectile Roll Dynamics
5a. CONTRACT NUMBER	
5b. GRANT NUMBER	
5c. PROGRAM ELEMENT NUMBER	
6. AUTHOR(S)	Jubaraj Sahu, Frank Fresconi, and Karen R. Heavey
5d. PROJECT NUMBER	AH80
5e. TASK NUMBER	
5f. WORK UNIT NUMBER	
7. PERFORMING ORGANIZATION NAME(S) AND ADDRESS(ES)	U.S. Army Research Laboratory ATTN: RDRL-WML-E Aberdeen Proving Ground, MD 21005-5069
8. PERFORMING ORGANIZATION REPORT NUMBER	ARL-TR-6997
9. SPONSORING/MONITORING AGENCY NAME(S) AND ADDRESS(ES)	
10. SPONSOR/MONITOR'S ACRONYM(S)	
11. SPONSOR/MONITOR'S REPORT NUMBER(S)	
12. DISTRIBUTION/AVAILABILITY STATEMENT	Approved for public release; distribution is unlimited.
13. SUPPLEMENTARY NOTES	

14. ABSTRACT

This report describes a computational study to understand the roll behavior of a canard-controlled projectile. Numerical computations were performed for this projectile with roll control maneuvers using advanced computational fluid dynamics and coupled aerodynamics/rigid body dynamics techniques. Roll control algorithms were formulated based on aerodynamic model assessment and parameter estimation. Coupled techniques were validated against wind tunnel (WT) experiments for roll control maneuvers. Overall, computed roll control results matched well with the WT test data; this indicated that the coupled calculations seem to capture the relevant physics observed in the experiment.

15. SUBJECT TERMS

coupled aerodynamics/flight dynamics, virtual fly-outs, guided, roll control, validation

16. SECURITY CLASSIFICATION OF:			**17. LIMITATION OF ABSTRACT**	**18. NUMBER OF PAGES**	**19a. NAME OF RESPONSIBLE PERSON**
					Jubaraj Sahu
a. REPORT	**b. ABSTRACT**	**c. THIS PAGE**			**19b. TELEPHONE NUMBER** (*Include area code*)
Unclassified	Unclassified	Unclassified	UU	54	410-306-0798

Standard Form 298 (Rev. 8/98)
Prescribed by ANSI Std. Z39.18

Contents

List of Figures

List of Tables

Acknowledgments

This work was accomplished as part of a grand challenge project jointly sponsored by the Department of Defense High Performance Computing Modernization program and the U.S. Army Research Laboratory. The author also wishes to thank Dr. Sukumar Chakravarthy of Metacomp Technologies for providing expert advice and help with the coupled computational fluid dynamics/rigid body dynamics/flight control system virtual fly-out simulations.

INTENTIONALLY LEFT BLANK.

1. Introduction

Course correction is an essential element of any guided weapon; therefore, understanding maneuvering projectile flight behaviors is critical. Ballistic flight of symmetric projectiles is well documented in the literature (*1–3*). Aerodynamic characterization techniques include semi-empirical, wind tunnel (WT), spark range, and computational fluid dynamics (CFD). Rigid body flight dynamics often utilize aerodynamic coefficients obtained using these techniques within an aerodynamic model framework. More recently, theoretical (*4–6*) and experimental (*7, 8*) studies proposed aerodynamic models for guided projectile flight. A major concern, especially when adding moveable aerodynamic surfaces (e.g., canards) upstream of the body or stabilizing fins, is flow interactions. The motion of upstream control surfaces at various aerodynamic angles of attack and Mach numbers greatly influences the pressure distribution on downstream surfaces. A significant body of literature, largely focused on the missile applications, has addressed the added complexity of canard-fin-body aerodynamics (*9–14*). A significant contribution to these studies would be shifting from multidimensional table look-ups based on exhaustive aerodynamic quantification to mathematical models, which inherently include effects captured in the multidimensional tables.

New computational techniques are being developed to understand flight behaviors of both unguided and guided projectiles by incorporating coupling between the projectile aerodynamics and the rigid body dynamics (RBD). This technique, known as coupled CFD/RBD or virtual flyout method, uses advanced CFD methods to characterize the unsteady aerodynamics at each instant in time. The forces and moments are inserted in the flight mechanics model to solve for the projectile state. The updated states (e.g., angle of attack, forward velocity) in turn change the CFD parameters for determining aerodynamic forces and moments at the next time step. This process marches forward in time from initial conditions to some termination criteria. This technique yields a wealth of data unavailable in experimental methods, but it does involve highly computer intensive calculations requiring large computational resources. Flow fields, pressure distributions on various surfaces, and the complete twelve-state RBD history are available. Coupled CFD/RBD simulations have been conducted and successfully validated on the ballistic flight of spin- and fin-stabilized projectiles (*15–19*). Significant capability has been added to the CFD/RBD technique recently by adding a flight control system (FCS) module for computation of controlled maneuvers in the simulations. Canard and jet maneuvers have been introduced and examined in coupled CFD/RBD/FCS simulations (*20–22*).

Guidance and flight control of projectiles (*8, 23–38*) and missiles (*39–44*) has been explored in depth in the literature. Of particular interest for this study are investigations into roll control. Isolating the controlled aeromechanics for the roll channel provides a better fundamental understanding for application to the full roll-pitch-yaw flight.

The novel contributions of this study include roll control design, validation of coupled simulation techniques, and aerodynamic modeling for guided projectiles. The report begins by describing advanced CFD and coupled CFD/RBD/FCS techniques, which are applied to a canard-controlled, fin-stabilized projectile to facilitate aerodynamic modeling and coupled flight simulations. A roll controller is formulated based on the aerodynamic model. Coupled CFD/RBD/FCS simulations were conducted with canard deflections derived from the roll controller. Parameter estimation was performed on the coupled CFD/RBD results and WT data to assess suitability of the aerodynamic model. Validation of the CFD/RBD/FCS simulations was made with available WT data. The following sections describe the standard virtual WT approach and coupled numerical procedure and the computed results obtained with roll control maneuver and validation with data.

2. Computational Strategy

Both steady-state CFD computations (virtual WT approach) and time-accurate coupled CFD/RBD virtual fly-out computations were performed using Navier-Stokes techniques for a canard-controlled projectile at Mach, M = 0.49. Steady-state computations were used to characterize the roll aerodynamics for input into the aerodynamic model. In the coupled calculations, unsteady aerodynamics and flight dynamics were computed simultaneously, and the roll response of the projectile was determined. In all cases, full three-dimensional (3-D) solutions were obtained and no symmetry was used. The primary interest was in the application and validation of the coupled CFD/RBD technique for accurate simulation of the free-flight aerodynamics and flight dynamics of the projectile with roll control maneuvers.

3. Model Geometry and Grid

The projectile modeled in this study is basically the same model that was tested in the WT (*8*). The length of the projectile is 403 mm and the main diameter is 80 mm. The computational model, as shown in figure 1, has a hemispherical nose, four canards and six fins. The main portion of the body consists of an 80-mm-diameter cylinder, which is followed by a conical section. The diameter is 103 mm just forward of the fins. Two configurations, 0° fin cant and 2° fin cant, were modeled; however, the primary focus in this study has been the 2° fin cant case. The experimental model was sting-mounted at the base of the projectile; therefore, the sting (although not shown in figure 1) was also included in the computational model.

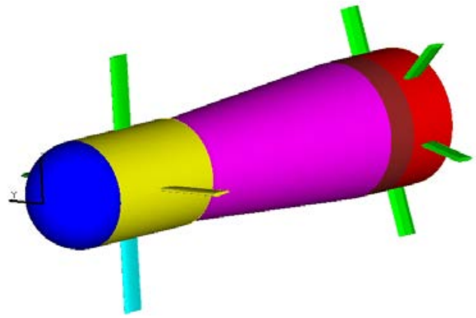

Figure 1. Computational model of the projectile geometry.

The grids for the computational models were created using GRIDGEN (*45*), a commercially available software package. A computer-aided design (CAD) file served as a starting point to provide the basic geometry. A structured mesh was created for the 2° fin cant model, using a zonal blocking strategy based on three unique sections: the main body, the canards and the fin area. This methodology facilitated grid block replacement for the two fin cants and the various canard configurations. The major portion of the computational mesh includes the body, fins, and a rear-mounted sting and consists of approximately 25 million cells. In general, most of the grid points were clustered in the boundary layer and the regions containing the nose canards and the afterbody fins. The boundary-layer spacing near the wall was selected such that a y+ value of 1.0 was achieved. The four nose canards were meshed separately, and consist of approximately 1.3 million cells each. These four canard meshes were then overset with the background projectile body mesh using the Chimera procedure (*46*). The final Chimera-overlapped mesh for each of the two (fin cant) models consists of approximately 30 million cells. An expanded view of the grid in the symmetry plane is shown in figure 2 for one of the models. This plane happens to be one that contains no fins in the plane, but it does show the rear sting. A circumferential cut in the vicinity of the canards (see figure 3) shows a cross-sectional view of the merged background and canard meshes. The outer boundaries of the canard meshes were chosen in a manner that required no cutting of the canard meshes by the main projectile body. However, the canards themselves were selected as cutters to cut holes in the background body mesh. The Chimera procedure requires proper transfer of information between the background mesh and the canard meshes at every time step. However, the advantage is that the individual grids are generated only once and the Chimera procedure can then be applied repeatedly as required during the canard motion. There is no need to generate new meshes at each time step during the canard roll control maneuvers.

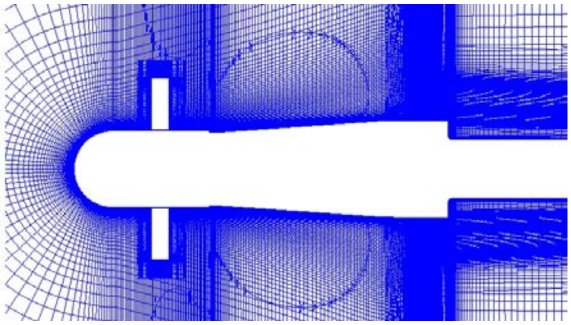

Figure 2. View of the mesh in the symmetry plane, near the body.

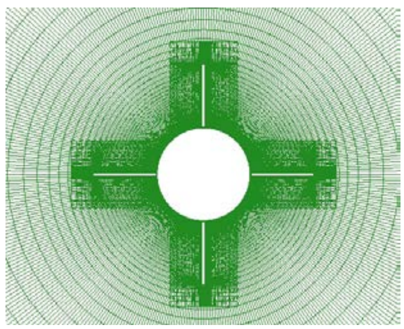

Figure 3. View of the mesh in the circumferential plane, near the canards.

4. Virtual Wind Tunnel Approach

4.1 Solution Technique

In the virtual WT approach, we use an advanced CFD Navier-Stokes computational technique. The complete set of 3-D time-dependent Navier-Stokes equations is solved in a time-asymptote manner to obtain converged steady-state solutions. A commercially available code, CFD++ (*47*, *48*) is used and the 3-D, time-dependent Reynolds-averaged Navier-Stokes equations are solved using the following finite volume method:

$$\frac{\partial}{\partial t}\int_V \mathbf{W}dV + \oint[\mathbf{F}-\mathbf{G}]\cdot dA = \int_V \mathbf{H}dV \tag{1}$$

where **W** is the vector of conservative variables, **F** and **G** are the inviscid and viscous flux vectors, respectively, **H** is the vector of source terms, *V* is the cell volume, and *A* is the surface area of the cell face.

Several techniques, such as implicit scheme and relaxation, are used to achieve faster convergence. Use of an implicit scheme circumvents the stringent stability limits suffered by their explicit counterparts, and successive relaxation allows update of cells as information becomes available and thus aids convergence. Second-order discretization was used for the flow variables and the turbulent viscosity equation. The turbulence closure is based on topology-parameter-free formulations. A realizable two-equation k-ϵ turbulence model (*49*) was used for the computation of turbulent flows. These models are ideally suited to unstructured book-keeping and massively parallel processing due to their independence from constraints related to the placement of boundaries and/or zonal interfaces.

4.2 Results

Steady-state computations were performed for a variety of flight conditions at M = 0.49: three angles of attack, –5°, 0°, and 5°; three aerodynamic roll angles, 0°, 22.5°, and 45°; and five canard deflections, –8°, –4°, 0°, 4°, and 8°. The definition of the aerodynamic angles is assisted through the illustration in figure 4. Positive canard deflection produces a counter-clockwise rolling motion when viewed from the base of the projectile.

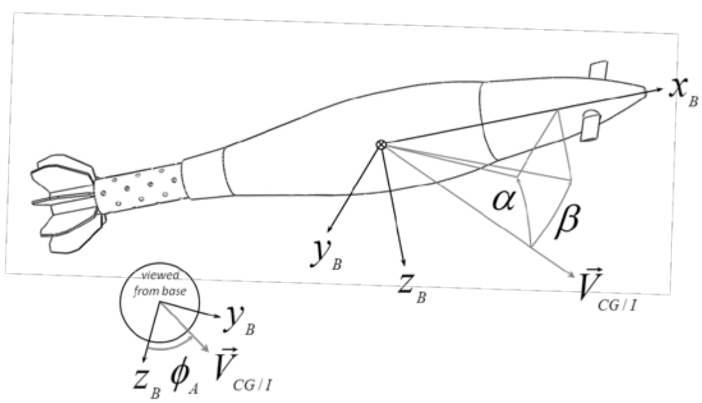

Figure 4. Body-fixed coordinate system and aerodynamic angles.

A few representative results obtained from these computations are shown in figures 5–7, which illustrate the computed surface pressure contours in the longitudinal plane for some of these cases. The same range of pressures from 5.0e +4 to 1.0e + 5 Pa is used in the contour plots in these figures. Higher pressures are shown in red and lower pressures in blue. The legend is the same for these three figures and is included in figure 5 only. Figure 5 shows the computed surface contours at 0° angle of attack and a 4° canard deflection. The surface pressures on the canards look the same at the three different roll angles from 0° to 45°. These results indicate that the roll moment is insensitive to the roll positions. Also, the surface pressure at the nose is symmetric as expected at 0° angle of attack and is high at the nose of the projectile.

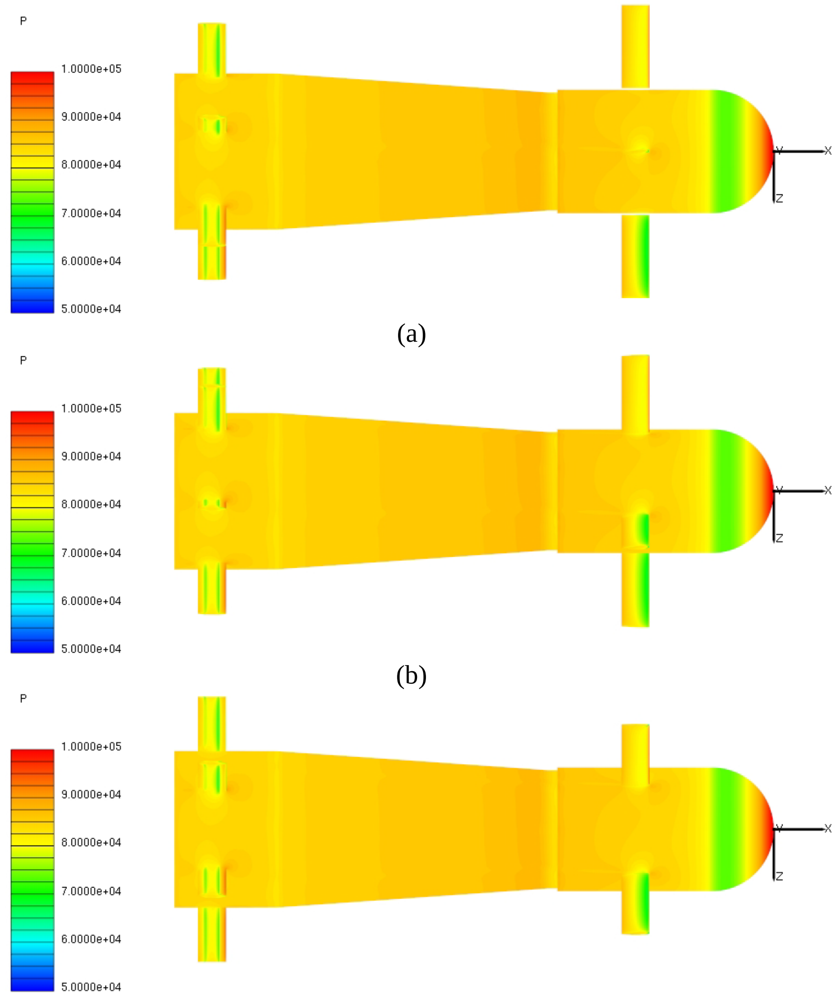

(a)

(b)

(c)

Figure 5. Computed surface pressure contours at α = 0° and canard deflection=4° for different roll positions, (a) 0°, (b) 22.5°, and (c) 45°. ($5.0e + 04 \leq P \leq 1.0e + 05$ Pa).

Figures 6 and 7 show the surface pressure contours at 0° roll and at angles of attack, α = –5° and 5°, respectively. Asymmetry in the flow field due to angle of attack is clearly seen in the nose region of the projectile; surface pressures are higher on the top surface and lower on the bottom surface at α = –5°, and the vice versa at α = 5°. The computed results show almost no change for most of the body between the canards and the fins as a function of canard deflections. The surface pressures on the canard themselves do show large differences as a function of canard deflections. As seen in these figures, the surface pressures on the two vertical canards are identical at 0° canard deflection, thus producing no roll. At negative canard deflections, the bottom vertical canard shows higher surface pressure than the top vertical canard, indicating a positive roll for these cases. The reverse is true for positive canard deflections. The flow field near one of the two horizontal canards, the right canard, can be seen in these figures. Clearly, the flow fields near the two horizontal canards are affected quite a bit by the canard deflections.

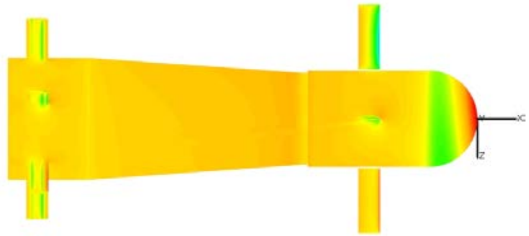

(a)

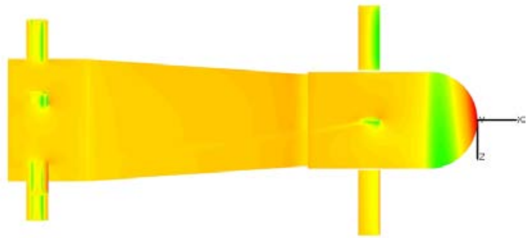

(b)

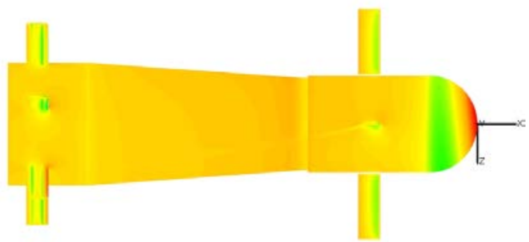

(c)

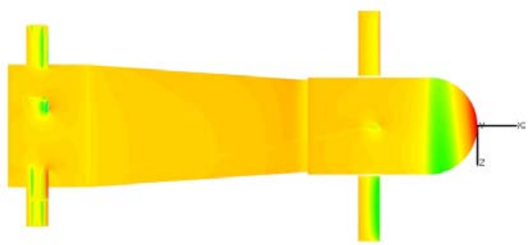

(d)

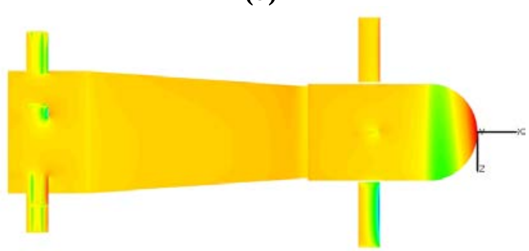

(e)

Figure 6. Computed surface pressure contours at $\alpha = -5°$ and roll = 0° for different canard deflections, (a) –8°, (b) –4°, (c) 0°, (d) 4°, and (e) 8°. ($5.0e + 04 \leq P \leq 1.0e + 05$ Pa).

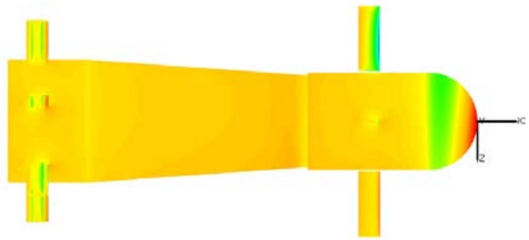

(a)

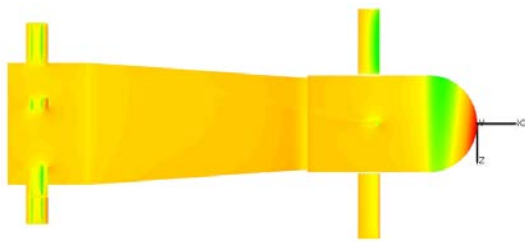

(b)

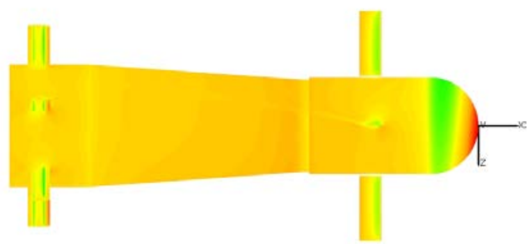

(c)

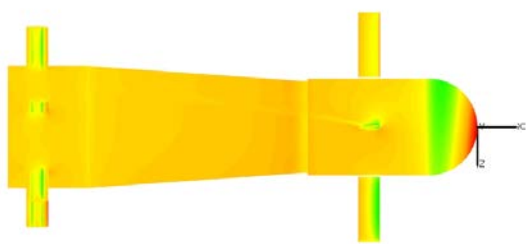

(d)

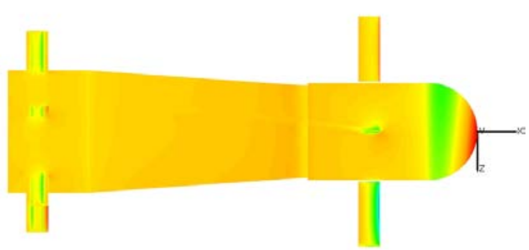

(e)

Figure 7. Computed surface pressure contours at $\alpha = 5°$ and roll = 0° for different canard deflections, (a) –8°, (b) –4°, (c) 0°, (d) 4°, and (e) 8°. ($5.0\text{ e }+04 \leq P \leq 1.0\text{e} + 05$ Pa).

With the freestream flow at an angle of attack, the deflection of the canards changes the local angle of attack for the horizontal canards. The local canard angle of attack varies from –13° in figure 6a to 3° in figure 6e; the flow field near the right horizontal canard for a canard deflection of 4° or with a local angle of attack of –1° is almost symmetric (see figure 6d). Similar behavior can be observed at α = 5° (see figure 7b) where the local canard angle of attack corresponds to +1°.

Figures 8 and 9 show the variation of the computed rolling moment coefficients with canard deflections at angles of attack, α = 0° and α = –5°, respectively. These figures also show results for the three different roll angles considered in this study. As seen in figure 8, the computed roll moment coefficient, C_l, shows no change as a function of roll position at α = 0°. However, as angle of attack is increased to 5°, there is a small effect of roll angle on the roll moment especially at higher canard deflections (see figure 9). The computed C_l becomes more and more negative with increasing canard defelction angle at both angles of attack, α = 0° and α = –5°. Figures 10 and 11 show the variation of computed rolling moment coefficient as a function of angle of attack and canard deflection, respectively for one roll position, ϕ = 0°. Also, shown here is an estimate of C_l from semi-empirical aeroprediction (PRODAS) at 0° angle of attack and zero canard deflection only for comparison purposes (*3*). The roll moment in this case is a result of the 2° fin cant. As expected, the rolling moment changes linearly with canard deflection at α = 0°; however, at angles of attack (α = –5° and 5°), one can begin to see nonlinear behavior at higher canard deflections (near 8°). These computed results were used in the developing an aerodynamic model for roll dynamics.

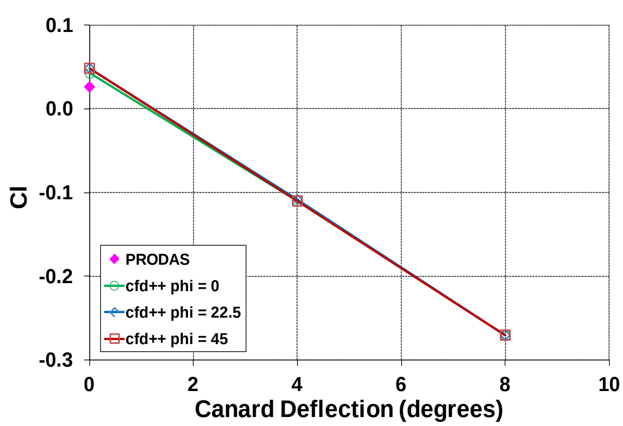

Figure 8. Computed roll moment coefficient, α = 0°.

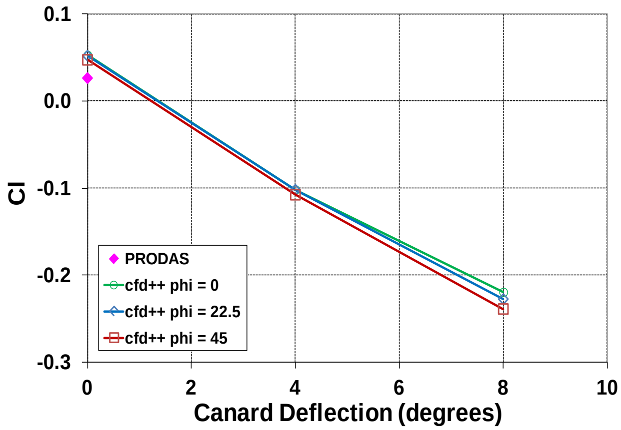

Figure 9. Computed roll moment coefficient, $\alpha = -5°$.

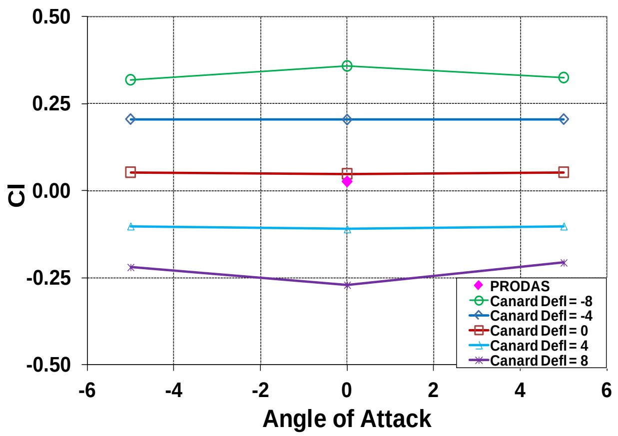

Figure 10. Computed roll moment coefficient, ϕ= 0° (angle of attack).

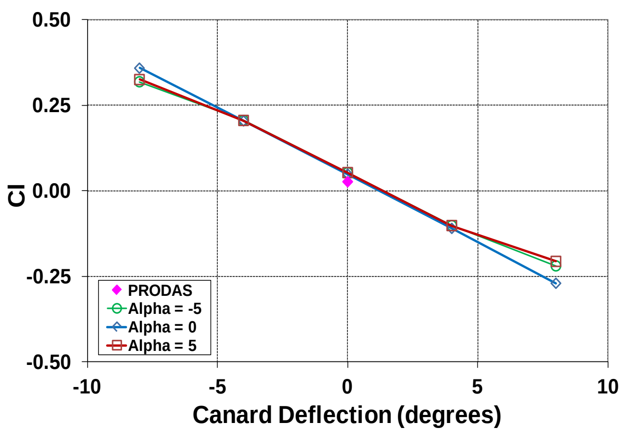

Figure 11. Computed roll moment coefficient, ϕ = 0° (canard deflection).

5. Coupled CFD/RBD With Flight Control Approach

5.1 Solution Technique

Research efforts are ongoing to perform time-accurate multidisciplinary coupled CFD/RBD computations for complex guided projectiles. With or without flight control, the coupled CFD/RBD procedure allows “virtual fly-out” of projectiles on the supercomputers and the prediction of actual flight paths of a projectile and all the associated unsteady free-flight aerodynamics in an integrated manner. A time-accurate numerical approach is used in the coupled virtual fly-out simulations. This approach requires that the 6-degrees-of-freedom (6DOF) body dynamics be computed at each repetition of a flow solver. The CFD capability used here solves the same Navier-Stokes equations shown in equation 1 and incorporates advanced boundary conditions and grid motion capabilities. For time-accurate simulations of virtual fly-outs that are of interest here, a dual time-stepping procedure was used to achieve the desired time accuracy in the time-accurate solutions. The whole grid was moved to take into account the motion of the projectile. To account for RBD, the grid point velocities were set as if the grid is attached to the rigid body with 6DOF.

As stated earlier, the 6DOF available to a rigid body projectile in free-flight for this problem reduces to a consideration of roll. The equation of motion for the projectile roll is shown.

$$I_X \ddot{\phi} = L \tag{2}$$

This equation is numerically integrated forward in time to obtain the roll rate response. The roll angle history is calculated by simple integration of the roll rate. The rolling motion of this projectile configuration is driven by moments due to fin cant, deflected canards, and roll damping which will be described later with an aerodynamic model.

For simulations of guided control maneuvers, a procedure that integrates flight control into the coupled CFD/RBD method is used (*4*). In the present work, canards are deflected to generate aerodynamic moments required to control the projectile roll. A flight control algorithm uses feedback from the RBD integration to supply the deflection commands and a dynamic model of the actuator translates commands into actual deflection angles. Inspection of experimental responses with low-cost servomechanisms shows that actuator dynamics can be described using a first-order system with a delay and bias. The mathematical model is given in the following equation

$$\tau \dot{\delta}(t) + \delta(t) = \delta_C(t - t_D) + \delta_B \tag{3}$$

Thus, the coupling can be summarized as follows: The canard deflection output of the flight control element is used to move the grid (locations and velocities) for the next CFD time step computation. CFD computes the aerodynamic moment which dictates the projectile flight motion and subsequent controlled deflections.

Typically, the coupled solution procedure requires three steps. First, we begin with a computation performed in the "steady-state mode" with the grid velocities prescribed to account only for the translational motion component of the complete set of initial conditions. At the second step, we also impose the angular orientations from the initial conditions and spin rate is added for spinning projectiles. Computations are performed with the spin in a time-accurate mode for a desired number of spin cycles. Converged solution from this second step provides the initial condition for the third step. In the third step, the remaining rotational velocity components (pitch and yaw) are added and a completely coupled CFD/RBD computation is performed in time-accurate mode. The solution from the third step should correspond to the complete set of initial conditions that includes all translational and rotational velocity components and accounts for initial position and angular orientations. In addition, flight control is activated at the beginning of this coupled run for guided flights.

6. Aerodynamics Modeling

The aerodynamic roll moment consist of roll producing terms from the fins and canards along with roll damping.

$$L = \bar{q}SD\left[C_l^F + C_l^C + \frac{DC_{l_p}}{2V}\dot{\phi}\right] \tag{4}$$

The functional form of the roll producing moment of the fins was established using virtual WT CFD data. Figure 12 provides the roll moment coefficient of the fins for a given aerodynamic roll angle as a function of angle of attack and canard deflection angle. All four canards were deflected to the same angle for these computations.

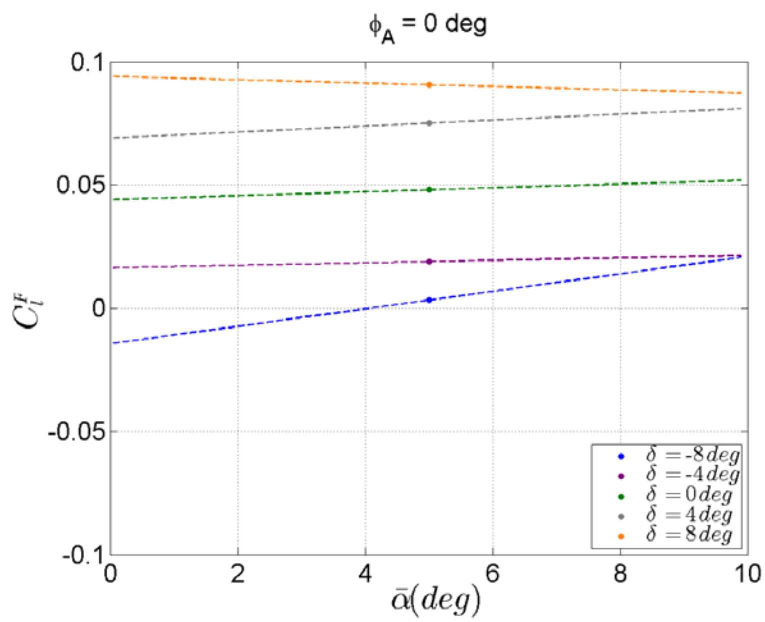

Figure 12. Fin roll producing moment coefficient.

These data clearly indicate a trend with canard deflection and a more moderate dependence on angle of attack. The form of the aerodynamic model for fin roll producing moment follows.

$$C_l^F = C_{l_0}^F(\delta) + C_{l_{\bar{\alpha}}}^F(\delta)\bar{\alpha} \tag{5}$$

Prior to examining the aerodynamics of the canards, a few definitions are provided. The flow velocity at the canard is different than the flow velocity at the projectile due to the angular velocity of the projectile. The expression for velocity at a general canard or moveable aerodynamic surface location for a body in arbitrary motion is given.

$$\begin{bmatrix} u_{M_i}^B \\ v_{M_i}^B \\ w_{M_i}^B \end{bmatrix} = \begin{bmatrix} u \\ v \\ w \end{bmatrix} + \begin{bmatrix} p \\ q \\ r \end{bmatrix} \times D \begin{bmatrix} \left(CP_X\left(M, \delta_{C_i}\right) + CG_N - CG_{N,A}\right) \\ CP_R cos\left(\phi_{M_i}\right) \\ CP_R sin\left(\phi_{M_i}\right) \end{bmatrix} \tag{6}$$

Aerodynamic angles are expressed in the body-fixed coordinate system. A local moveable aerodynamic surface coordinate system is useful for a generalized assessment of aerodynamics of the canards. The body-fixed and moveable aerodynamic surface coordinates are related by a transformation matrix.

$$\vec{T}_{BM_i} = \begin{bmatrix} 1 & 0 & 0 \\ 0 & cos\left(\phi_{M_i}\right) & sin\left(\phi_{M_i}\right) \\ 0 & -sin\left(\phi_{M_i}\right) & cos\left(\phi_{M_i}\right) \end{bmatrix} \tag{7}$$

Transforming velocities from the body-fixed coordinates into the moveable aerodynamic surface coordinates permits calculation of local angle of attack at each canard.

$$\begin{bmatrix} u_{M_i}^{M_i} \\ v_{M_i}^{M_i} \\ w_{M_i}^{M_i} \end{bmatrix} = \vec{T}_{BM_i} \begin{bmatrix} u_{M_i}^{B} \\ v_{M_i}^{B} \\ w_{M_i}^{B} \end{bmatrix} \quad (8)$$

$$\alpha_{M_i} = \delta + asin\left[\frac{w_{M_i}^{M_i}}{\sqrt{{u_{M_i}^{M_i}}^2 + {w_{M_i}^{M_i}}^2}}\right] \quad (9)$$

The roll-inducing moment from each canard was assessed with virtual WT CFD methods. These data are shown in figures 13–15. At 0° projectile body angle of attack with all canards deflected to –8°, –4°, 0°, 4°, and 8°, a linear fit with local angle of attack matches the data points. At projectile body angles of attack off 0°, the nonlinearities with local moveable aerodynamic surface angle of attack are apparent. All canard aerodynamic data suggest reflective symmetry when comparing results at positive and negative deflection or positive and negative projectile body angle of attack. Based on inspection of these data, the following model for the canard roll moment coefficient is proposed.

$$C_l^C = C_{l_0}^C(\delta) + C_{l_{\alpha_{M_i}}}^C(\delta)\alpha_{M_i} + C_{l_{\alpha_{M_i}^3}}^C(\delta)\alpha_{M_i}^3 + C_{l_{\alpha_{M_i}^5}}^C(\delta)\alpha_{M_i}^5 \quad (10)$$

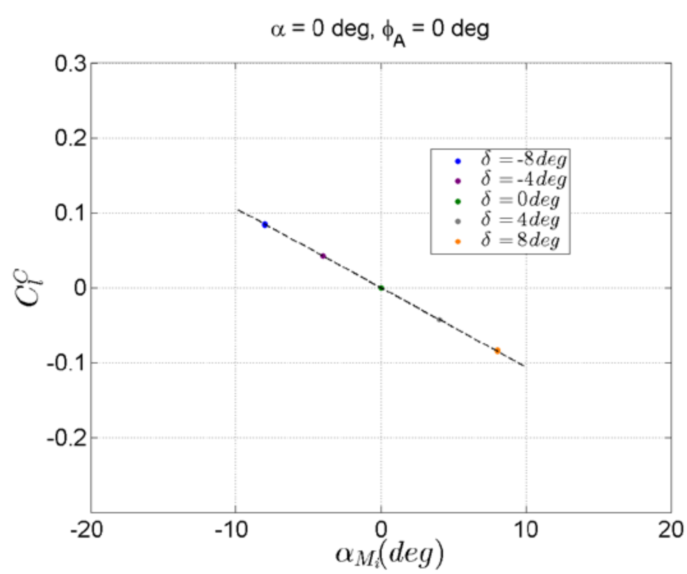

Figure 13. Canard roll producing moment coefficient at 0° projectile angle of attack.

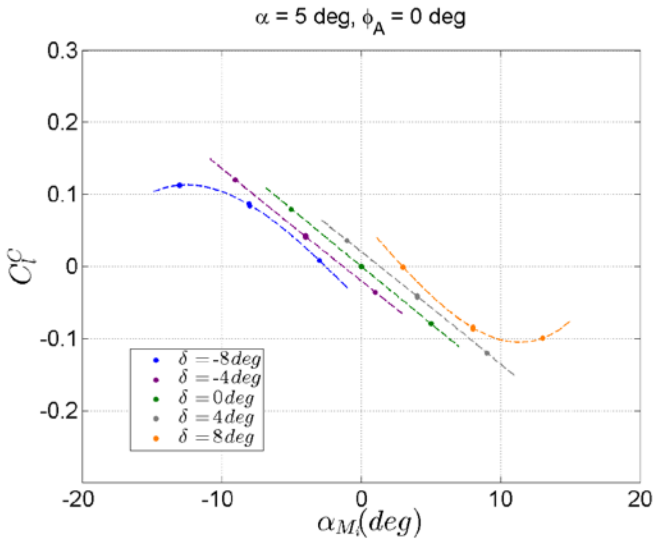

Figure 14. Canard roll producing moment coefficient at 5° projectile angle of attack.

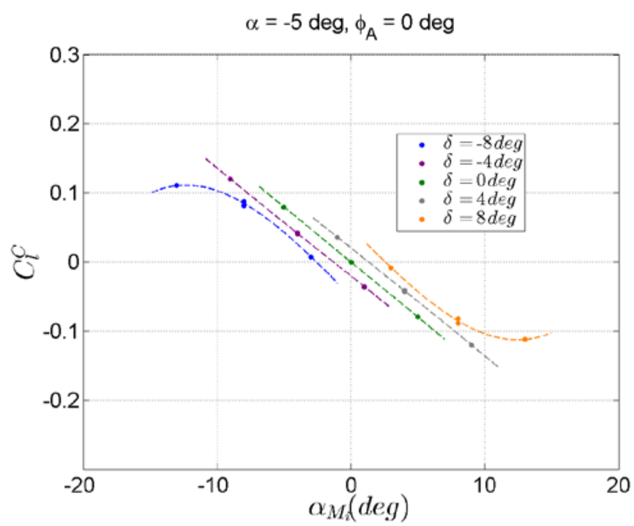

Figure 15. Canard roll producing moment coefficient at –5° projectile angle of attack.

The roll-damping moment coefficient shown in equation 4 represents contributions from the projectile body and fins. Roll damping from the canards is not included in that coefficient since the aerodynamic model formulation for the canards implicitly models damping effects (i.e., through the cross-product term in the equation to determine the velocity at the moveable aerodynamic surface).

The aerodynamic coefficients from the virtual WT CFD predictions that populate the aerodynamic model are tabulated in table 1.

Table 1. Aerodynamic coefficients from virtual WT CFD data.

Coefficients	$\boldsymbol{\delta = -8\,°}$	$\boldsymbol{\delta = -4\,°}$	$\boldsymbol{\delta = 0\,°}$	$\boldsymbol{\delta = 4\,°}$	$\boldsymbol{\delta = 8\,°}$
$C_{l_0}^F$	–0.014441	0.016381	0.044016	0.069039	0.094026
$C_{l_{\bar{\alpha}}}^F$	0.202975	0.028758	0.045551	0.069109	–0.038995
$C_{l_0}^C$	–0.049521	–0.020236	0.000001	0.020229	0.057299
$C_{l_{\alpha_{M_i}}}^C$	–1.120113	–0.883520	–0.912226	–0.883484	–1.203865
$C_{l_{\alpha_{M_i}}^3}^C$	7.959795	–0.383438	–0.006417	–0.379916	9.412987
C_{l_p}	–1.8526				

7. Flight Control

This aerodynamic model facilitates control design. The basic feedback structure is illustrated in figure 16. The transfer function for the system dynamics ($\vec{H}$) includes models for the roll and actuator dynamics. A state space representation was used for control design. The states are roll, roll rate, and canard deflection ($\vec{x} = [\phi \quad \dot{\phi} \quad \delta]^T$), and the control is deflection command ($u = \delta_C$). The aerodynamic model was linearized by assuming small angle of attack and removing the deflection dependence in the fin and canard roll moment. The time delay and bias in the actuator model were assumed negligible. This linearization results in a state transition matrix of the form:

$$\vec{A} = \begin{bmatrix} 0 & 1 & 0 \\ 0 & \dfrac{\bar{q}SD^2C_{l_p}}{2VI_X} & \dfrac{\bar{q}SDN_C C_{l_{\alpha_{M_i}}}^C}{I_X} \\ 0 & 0 & -1/\tau \end{bmatrix} \tag{11}$$

The controls matrix is as equation 12.

$$\vec{B} = \begin{bmatrix} 0 \\ 0 \\ 1/\tau \end{bmatrix} \tag{12}$$

The roll-inducing moment of the fin adds a forcing function.

$$\vec{F} = \begin{bmatrix} 0 \\ \dfrac{\bar{q}SDC_{l_0}^F}{I_X} \\ 0 \end{bmatrix} \tag{13}$$

The measurement output is roll and roll rate ($\vec{y} = [\phi \quad \dot{\phi}]^T$), which yields the following measurement matrix.

$$\vec{C} = \begin{bmatrix} 1 & 0 & 0 \\ 0 & 1 & 0 \end{bmatrix} \tag{14}$$

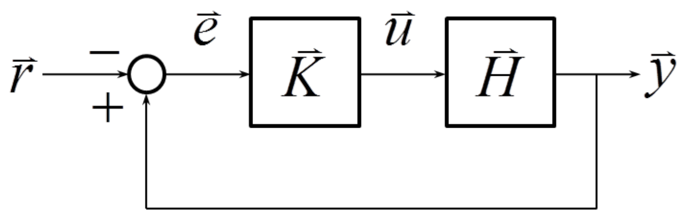

Figure 16. Block diagram of feedback control system.

The reference ($\vec{r}$) is combined with the feedback measurements to construct the control error signal ($\vec{e}$). The reference and error are shaped based on the desired performance. The goal of the control is to achieve zero roll rate and regulate roll angle to any of four configuration symmetry locations ($N_\phi = 4$). Four roll symmetry angles result from this four canard configuration. The roll error was constructed with the following expression.

$$e_\phi = \begin{cases} \left(\phi \ modulo \ \dfrac{2\pi}{N_\phi}\right) - \dfrac{\pi}{N_\phi} & if \ \phi \ modulo \ \dfrac{4\pi}{N_\phi} < \dfrac{2\pi}{N_\phi} \\ -\left(\phi \ modulo \ \dfrac{2\pi}{N_\phi}\right) + \dfrac{\pi}{N_\phi} & if \ \phi \ modulo \ \dfrac{4\pi}{N_\phi} \geq \dfrac{2\pi}{N_\phi} \end{cases} \tag{15}$$

The control technique was selected based on the linear actuator and roll dynamics, measurement models, and the feedback control structure presented. A linear quadratic regulator, derived using optimal control theory (*50*), was chosen for determining the gain matrix (K). In this formulation, the control minimizes a cost function.

$$J = \int_0^\infty \left(\vec{e}^T \overrightarrow{\mathbf{Q}} \vec{e} + u^T \mathbf{R} u\right) dt \tag{16}$$

The weightings for the tracking error $\overrightarrow{\mathbf{Q}}$ and control effort $\mathbf{R}$ are positive semi-definite and allow the designer to balance tracking of each desired state with specific control demand. Minimization of the cost function results in

$$u = \text{-}\vec{K}\vec{e} \tag{17}$$

The gain matrix can be found through the control effort weighting, the controls matrix, and the matrix $\vec{P}$.

$$\vec{K} = \mathbf{R}^{-1}\vec{B}^T\vec{P} \tag{18}$$

The $\vec{P}$ matrix is obtained by solving the algebraic matrix Riccati equation.

$$\vec{A}^T\vec{P} + \vec{P}\vec{A} - \vec{P}\vec{B}\mathbf{R}^{-1}\vec{B}^T\vec{P} + \vec{\mathbf{Q}} = 0 \tag{19}$$

---

8. Parameter Estimation

8.1 Technique

Nonlinear parameter estimation was conducted using a maximum likelihood method (*51–55*). This technique seeks to find model parameters which minimize a likelihood function.

$$\mathcal{L} = \frac{1}{(2\pi)^{\frac{N_M}{2}}\sqrt{\vec{\mathbb{R}}}} exp\left(-\frac{1}{2}\vec{\epsilon}^T\vec{\mathbb{R}}^{-1}\vec{\epsilon}\right) \tag{20}$$

The residuals are based on differencing the measurements and theoretical model predictions ($\vec{\epsilon} = \vec{x}_M - \vec{x}_C$). The residual covariance is a measure of the expected errors ($\vec{\mathbb{R}} = E[\vec{\epsilon}\vec{\epsilon}^T]$). The roll rate measurements ($\vec{x}_M$) were obtained from coupled CFD/RBD simulations or WT experiments. The number of measurement samples is N_M. For parameter estimation purposes, the predicted state is the roll rate ($\vec{x}_C = \dot{\phi}$) and the control is the deflection ($u = \delta_C$). Parameters are defined by re-expressing the previously stated aerodynamic models with a scaling factor which adjusts the aerodynamic coefficients so that the theoretical predictions of roll rate better match the measurements. Thus, the baseline aerodynamic coefficients obtained from the virtual WT CFD data were scaled according to the parameter adjustments resulting from aligning measurements to calculations in the parameter estimation algorithm.

The aerodynamic model used in the parameter estimation for fin roll moment is

$$C_l^F = f_{C_{l_0}^F} C_{l_0}^F(\delta) + f_{C_{l_{\bar{\alpha}}}^F} C_{l_{\bar{\alpha}}}^F(\delta)\bar{\alpha} \tag{21}$$

Similarly, for parameter estimation the canard roll moment is modeled with the following expression.

$$C_l^C = f_{C_{l_0}^C} C_{l_0}^C(\delta) + f_{C_{l_{\alpha_{M_i}}}^C} C_{l_{\alpha_{M_i}}}^C(\delta)\alpha_{M_i} + f_{C_{l_{\alpha_{M_i}^3}}^C} C_{l_{\alpha_{M_i}^3}}^C(\delta)\alpha_{M_i}^3 + f_{C_{l_{\alpha_{M_i}^5}}^C} C_{l_{\alpha_{M_i}^5}}^C(\delta)\alpha_{M_i}^5 \tag{22}$$

Lastly, the body-fin roll-damping moment model is provided.

$$C_{l_p} = f_{C_{l_p}} C_{l_p} \tag{23}$$

The parameter vector was formulated given these models.

$$\vec{\theta} = \begin{bmatrix} f_{C_{l_0}^F} & f_{C_{l_{\bar{\alpha}}}^F} & f_{C_{l_0}^C} & f_{C_{l_{\alpha_{M_i}}}^C} & f_{C_{l_{\alpha_{M_i}^3}}^C} & f_{C_{l_{\alpha_{M_i}^5}}^C} & f_{C_{l_p}} & f_{L_\mu} \end{bmatrix}^{\mathrm{T}} \tag{24}$$

The last term in the parameter vector was used to estimate friction existent in some of the experiments. A nonlinear Coulomb model incorporating static and dynamic friction was utilized, which was added as an additional moment in equation 2.

$$L_\mu = f_{L_\mu} sgn(\dot{\phi}) f\left(|\dot{\phi}|\right) \tag{25}$$

The roll dynamics and nonlinear aerodynamic model augmented with the parameter vector described previously were integrated forward in time during the parameter estimation process. Initial measurements and controls were used as the initial conditions for propagating the models. When times were reached where measurements were available, a Newton-Raphson method optimized the likelihood function. The residual and Jacobian ($\frac{\partial \vec{x}_C}{\partial \vec{\theta}}$) were calculated.

$$\frac{\partial \vec{x}_C}{\partial \vec{\theta}} = \begin{bmatrix} \frac{\partial x_{C_1}}{\partial \theta_1} & \frac{\partial x_{C_2}}{\partial \theta_2} & \cdots \\ \frac{\partial x_{C2}}{\partial \theta_1} & \ddots & \vdots \\ \vdots & \cdots & \frac{\partial x_{C_{N_M}}}{\partial \theta_{N_P}} \end{bmatrix} \tag{26}$$

The number of parameters is N_P. Forward differencing was applied to determine the Jacobian.

Parameters were corrected and applied to update the parameter estimates. The Levenberg-Marquardt method ($\xi \vec{I}$ term) was implemented to improve the conditioning of the information matrix ($\sum_{i=1}^{N_M} \frac{\partial \vec{x}_{C,i}}{\partial \vec{\theta}}^T \overline{\mathbb{R}}^{-1} \frac{\partial \vec{x}_{C,i}}{\partial \vec{\theta}}$ term) for the matrix inverse operation.

$$\Delta\vec{\theta} = \left(\sum_{i=1}^{N_M} \frac{\partial \vec{x}_{C,i}}{\partial \vec{\theta}}^T \overrightarrow{\mathbb{R}}^{-1} \frac{\partial \vec{x}_{C,i}}{\partial \vec{\theta}} + \xi \vec{I} \right)^{-1} \sum_{i=1}^{N_M} \frac{\partial \vec{x}_{C,i}}{\partial \vec{\theta}}^T \overrightarrow{\mathbb{R}}^{-1} \vec{\epsilon}_i \tag{27}$$

$$\vec{\theta}^{j+1} = \vec{\theta}^{j} + \Delta\vec{\theta} \tag{28}$$

The model was integrated again with the updated parameters and the residual was recalculated.

$$\dot{\vec{x}}_C = f\left(\vec{x}_C, u; \vec{\theta}^{j+1}\right) \tag{29}$$

This process was iterated at each measurement update until some convergence criterion (e.g., magnitude of residual below some threshold) was reached. On convergence, the updated parameter estimates were used during model integration until the next measurement update. Calculated response and parameter estimates were obtained over the entire measurement history.

8.2 Observability

The observability map of the nonlinear system was assessed to verify that the parameters under investigation were distinguishable. The types of questions that this analysis answers include whether a unique combination of fin roll moment and roll damping, for example, yield a particular roll rate history.

Consider the roll parameter estimation problem as outlined in this application. The roll history obtained from the measurements includes information about the roll rate at various times and also the roll acceleration at a given time. Mathematical expressions for these basic data included in the measurements are utilized in the formalism of constructing the observability map.

The first expression needed to assemble the observability map is the derivative of roll acceleration. The chain rule must be applied for each parameter for a total of nine terms in the following equation.

$$\dddot{\phi} = \frac{d\ddot{\phi}}{d\theta_i} \frac{d\theta_i}{dt} \tag{30}$$

An expression for the roll acceleration was provided in equation 2. Both equations for the derivative of roll acceleration and roll acceleration feature the roll moment, which includes complex relationships for the parameters as outlined in equations 4, 6–9, and 21–23.

Now, to construct the observability map a 2-by-2 matrix ($\Theta_{\theta_i \theta_j}$) is formed based on partial derivatives of the roll acceleration and roll acceleration equation with respect to parings of the parameters. An example for the zeroth-order fin roll moment and roll-damping moments is given.

$$\Theta_{\theta_1\theta_7} = \begin{bmatrix} \dfrac{\partial \dot{\phi}}{\partial f_{C^F_{l_0}}} & \dfrac{\partial \dot{\phi}}{\partial f_{C_{l_p}}} \\ \dfrac{\partial \ddot{\phi}}{\partial f_{C^F_{l_0}}} & \dfrac{\partial \ddot{\phi}}{\partial f_{C_{l_p}}} \end{bmatrix} \tag{31}$$

There are 9 parameters that yield 36 combinations $\binom{9}{2}$ for the matrix. Each of these matrices must be populated and the determinant calculated. If the determinant is zero (singular $\Theta_{\theta_i\theta_j}$) then that pairing is indistinguishable over the state space. In this situation, one of the indistinguishable parameters should be removed from the estimation process. While some practical limitations have not been addressed, performing this analysis over the entire parameter space provides some formal proof for which parameters are theoretically observable for a given problem. The observability map was constructed for each parameter pairing and all parameters were observable except for the following two pairings: $C^F_{l_0}$ and $C^C_{l_0}$, and $C^F_{l_{\bar{\alpha}}}$ and $C^C_{l_{\alpha_{M_i}}}$. These two pairings are theoretically indistinguishable and a unique value for each independently will not be sought in this report.

8.3 Results

Table 2 shows the cases executed in the parameter estimation routine. A variety of projectile body angle of attack, bearing friction, and deflection values were investigated. Measurements were provided from CFD/RBD simulations or WT experiments. More information on the WT experiments can be found in Fresconi et al. (*8*). The goal of the different cases was to isolate and quantify different phenomena; comments in the table refer to the specific effects that were under investigation.

Case 1 represents a roll-down of the projectile from an initial spin rate of 10 Hz to the steady-state spin rate. It featured 0° angle of attack, no bearing friction, and no control deflections. The intent of this case was to focus on quantifying the roll-damping moment, fin roll moment at 0° angle of attack, and canard roll moment. Measurements consisted of CFD/RBD data. Figure 17 shows the decrease in roll rate from 10 Hz initially to about 4 Hz by 1.5 s due to the balance of roll inducing fin cant and roll-damping moment. The calculations of roll rate resulting from adjusting the parameters to match the measurements are shown in the figure. Comparing the measured and calculated roll rate suggests that the aerodynamic model formulated for this configuration may be appropriate when considering coupled CFD/RBD simulation results. The average fit error (ϵ) was less than 0.1 Hz for this case.

Table 2. Parameter estimation cases at Mach 0.49.

Case	Measurement	α (°)	Bearing Friction	Control	Comments
1	CFD/RBD	0	off	off	Assess fin roll moment ($C_{l_0}^F$), roll-damping moment (C_{l_p}), and canard roll moment ($C_{l_{\alpha_{M_i}}}^C$)
2	CFD/RBD	0	off	closed loop	Assess fin roll moment ($C_{l_0}^F$), roll-damping moment (C_{l_p}), and canard roll moment ($C_{l_{\alpha_{M_i}}}^C$)
3	CFD/RBD	0	off	closed loop	Assess fin roll moment ($C_{l_0}^F$), roll-damping moment (C_{l_p}), and canard roll moment ($C_{l_{\alpha_{M_i}}}^C$)
4	WT	0	on	open loop	Assess bearing friction (L_μ), fin roll moment ($C_{l_0}^F$), roll-damping moment (C_{l_p}), and canard roll moment ($C_{l_{\alpha_{M_i}}}^C$)
5	WT	5.45	on	closed loop	Assess bearing friction (L_μ), fin roll moment ($C_{l_0}^F$, $C_{l_{\bar{\alpha}}}^F$), roll-damping moment (C_{l_p}), and canard roll moment ($C_{l_{\alpha_{M_i}}}^C$)

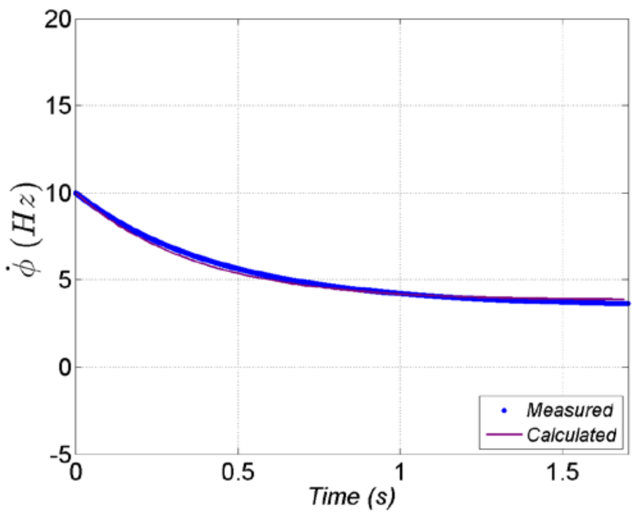

Figure 17. Measured and calculated roll rate for case 1.

In case 2, we have excited the system dynamics with canard deflections. Case 2 possessed 0° angle of attack, no bearing friction, and an initial roll rate of 10 Hz. Measurements were taken from coupled CFD/RBD simulations, which were conducted with closed loop deflections. The controller was a derivative of that outlined previously specifically designed to induce certain motions. Recall that the purpose of the current exercise is parameter estimation and not control performance. The deflections occurring as a result of roll angle and roll rate feedback are shown in figure 18. Measured deflections range from about –2° to 7°. The measured and calculated roll rates are presented in figure 19. Roll rate starts at 10 Hz and decreases to less than 1 Hz in 0.5 s. Again, the aerodynamic model seems to capture the dynamics evident in the coupled CFD/RBD simulations. The average fit error was about 0.3 Hz for this case.

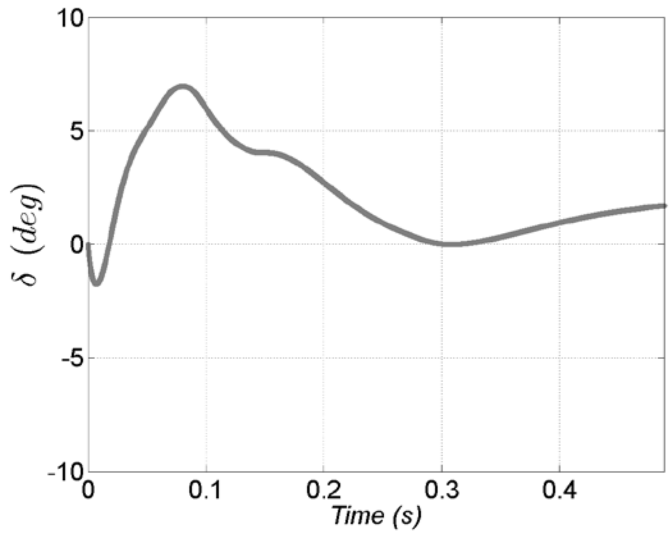

Figure 18. Deflections for case 2.

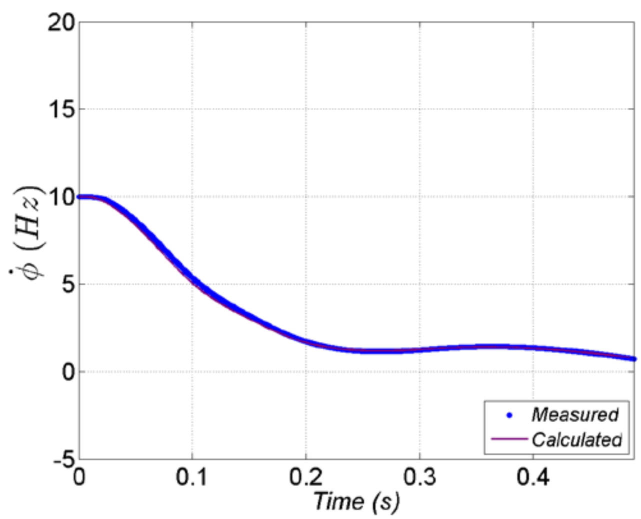

Figure 19. Measured and calculated roll rate for case 2.

Case 3 was similar to case 2 except the controlled deflections were altered somewhat. This case serves as a consistency check on the results of case 2. The measured deflection input, obtained from CFD/RBD simulations, is given in figure 20. The matching of the calculated to the measured response, shown in figure 21, yielded an average fit error amplitude of about 0.3 Hz. Recall that table 1 compiles parameters for all cases. The combined intent of cases 1–3 was to determine aerodynamic coefficients so that the effects of bearing friction could be more readily evaluated in cases 4 and 5.

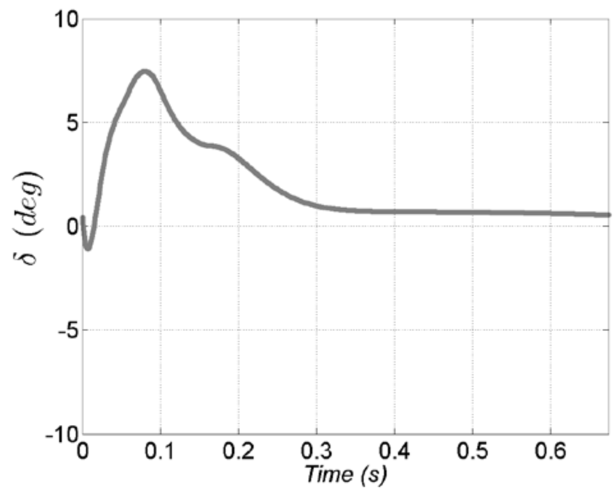

Figure 20. Deflections for case 3.

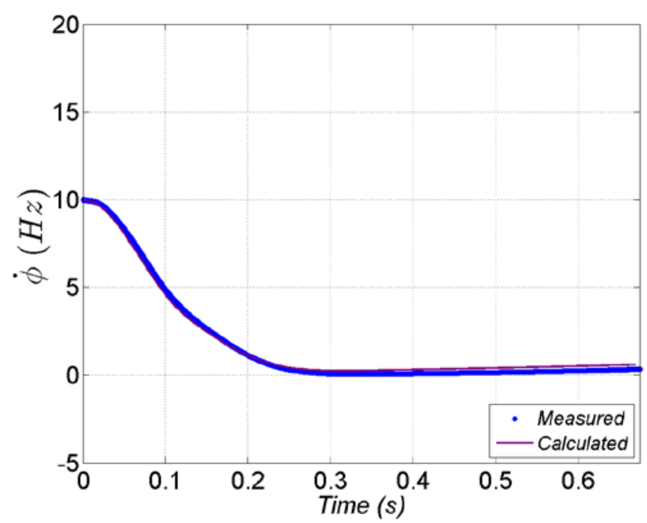

Figure 21. Measured and calculated roll rate for case 3.

Case 4 implemented WT data as the measurements. Experiments were conducted at 0° angle of attack. Bearing friction existed in the WT rig. Open loop control deflections whereby the deflection angle changed in 0.5° increments for a duration of 0.8 s each were performed. Measurements of all four canard deflections from a calibrated potentiometer are given in figure 22. The dots in this figure are individual measurements of all four canards. These data illustrate experimental scatter and canard-specific effects (e.g., bias, scale factor, noise). Regardless of the specific mechanism, these measurements were fed into the parameter estimation routine.

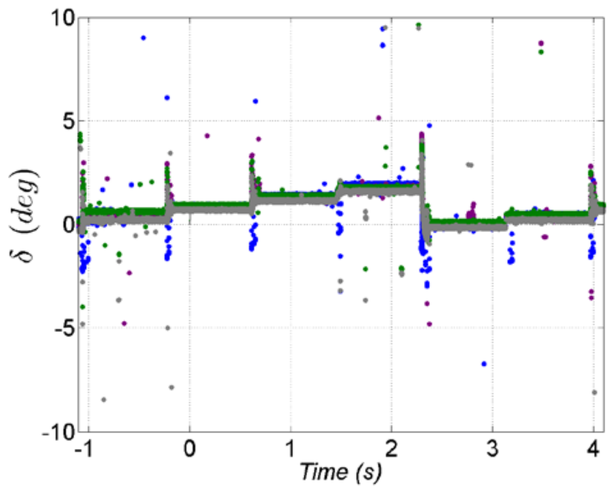

Figure 22. Deflections for case 4.

The measured and calculated roll rates are shown in figure 23 and the moments due to the fin, canard, and roll damping of the body-fin are shown in figure 24. Initially, the body is not rolling. The cant of the fins nominally produces a positive roll rate. The initial deflection angle of 0.5° would yield a negative roll rate in the absence of fin cant and bearing friction. The action of fin cant and bearing friction, however, keeps the roll rate at zero since the combined canard and bearing friction moments overwhelm the fin moment.

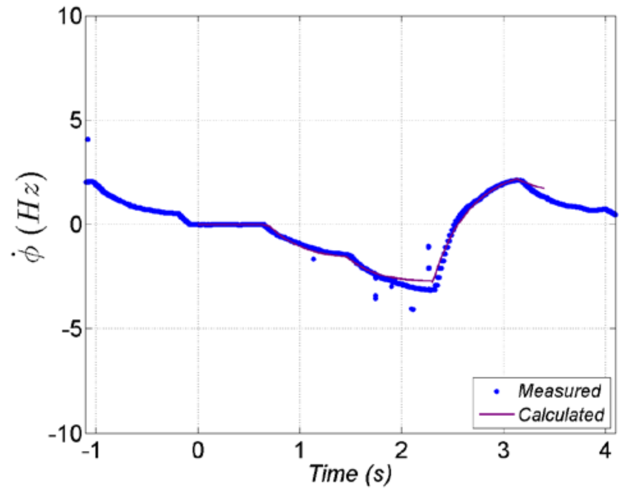

Figure 23. Measured and calculated roll rate for case 4.

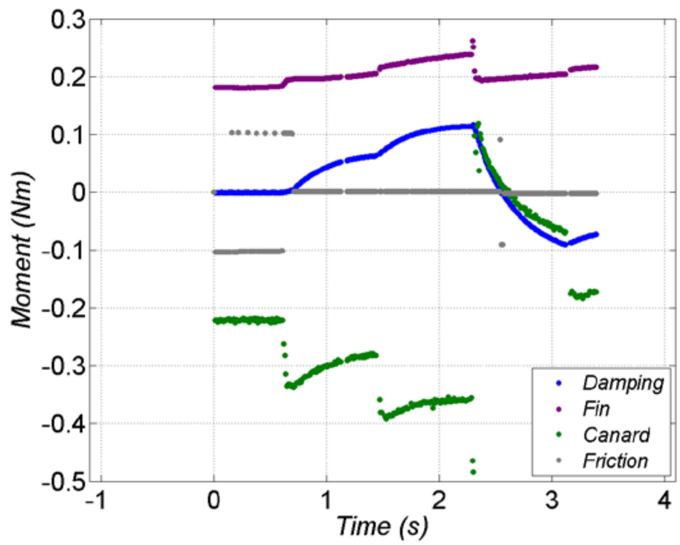

Figure 24. Calculated moments for case 4.

As deflection increases to 1° this balance of moments no longer exists. Canard moment overcomes the fin moment to produce a negative roll rate. This nonzero roll rate shifts the bearing friction from a high static to a low dynamic value and causes the body-fin roll damping to contribute.

An input step change in deflection to 1.5° results in a further negative roll rate. Roll-damping moment increases and bearing friction moment is still small.

When deflection is set back to 0° the fin cant dominates and induces positive projectile roll acceleration. Canard roll moment is due to the change in the local angle of attack due to the spin rate history (i.e., primarily a roll-damping mechanism) since deflection is zero. Body-fin roll-damping moment responds linearly with the roll rate. Bearing friction is small except for a short time duration when the roll rate passes through zero.

The influence of deflection angle on the fin and canard roll moment is evident in the moments of figure 24. These data also show that the experimental scatter in the deflections propagates into the calculated fin and canard roll moments.

The measured and calculated roll rates matched to within a 0.2-Hz average error. These results suggest that the aerodynamic model captures the relevant physics of the experiments in addition to retaining the key mechanisms implicit in the coupled CFD/RBD simulations.

Case 5 consisted of WT measurements (bearing friction active) at about 5° angle of attack with closed-loop control. The roll control algorithm was taken from the earlier description. Deflection histories are given in figure 25. The dots in this figure again are individual measurements of all four canards. In experiments, –8° deflections of all canards were commanded to increase the roll rate. When a 10-Hz threshold was reached, the closed loop controller was activated. Subsequently, larger positive deflections (about 9° maximum) were achieved prior to decreasing to less than 1° to counteract the fin cant within about 0.7 s.

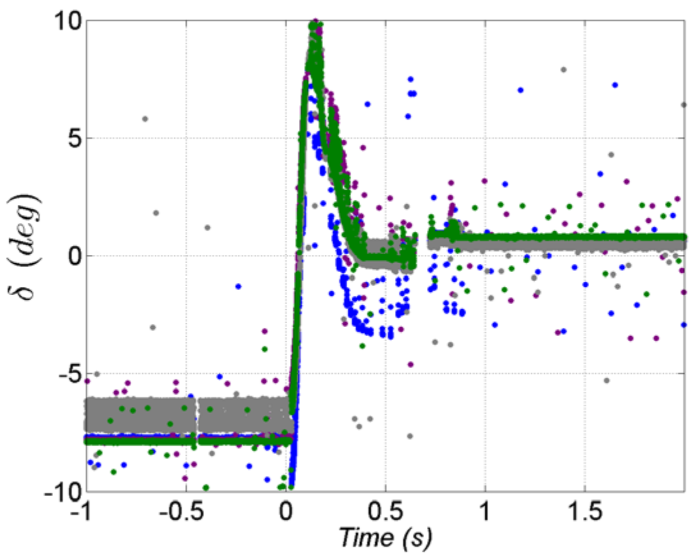

Figure 25. Deflections for case 5.

The measured and calculated roll rates and moments are provided in figures 26 and 27, respectively. Roll rate peaks past 11 Hz and was controlled to less than 1 Hz within 0.2 s. The canard roll moment dominates during this early portion of the roll control maneuver. At later times, the canard roll moment balances the fin roll moment. The fin roll moment varies slightly with deflection. The angle of attack dependency of the fin roll moment is also contained in these results since this case featured a 5° angle of attack. Body-fin roll-damping scales with the roll rate. Bearing friction is small except for short time durations when roll rate passes through zero and the static friction emerges.

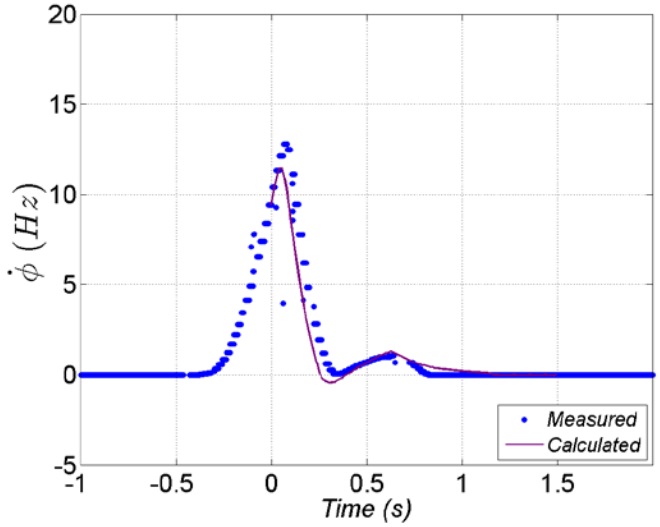

Figure 26. Measured and calculated roll rate for case 5.

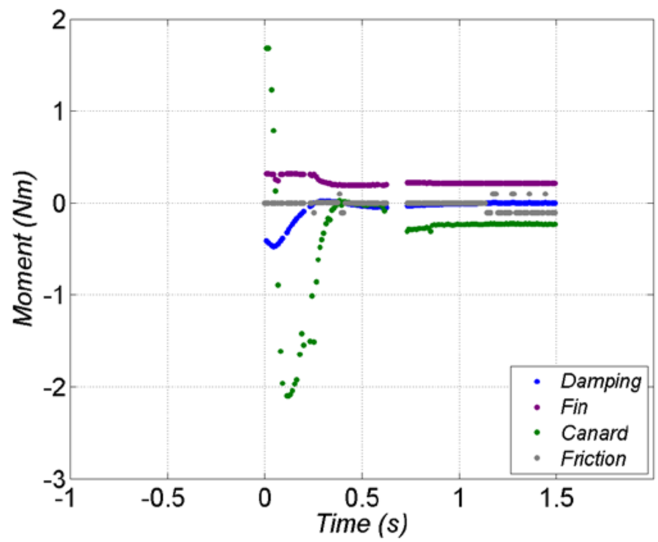

Figure 27. Calculated moments for case 5.

The average fit error between the measured and calculated roll moment was 0.2 Hz. These data provide more indication of the feasibility of the aerodynamic model to properly accommodate the relevant physics of the experiments.

A summary of data obtained from the parameter estimation process for all cases are included in table 3. Parameters with a value of 1 in the table were held constant in the analysis for that case. Overall, fit errors are low enough to suggest that the aerodynamic model appropriately handles the phenomena in the simulated and experimental flights. Comparing actual values derived from the different measurement sources demonstrates some variability due to modeling or measurement error. The fin roll moment for the experiments was consistently lower than that for the simulations likely due to the accuracy associated with setting the fin cant during experiments. Greater uncertainty is afforded to the bearing friction parameters due to limited experimental data.

Table 3. Parameter estimation data summary.

Case	$f_{C^F_{l_0}}$	$f_{C^F_{l_{\bar{\alpha}}}}$	$f_{C^C_{l_0}}$	$f_{C^C_{l_{\alpha M_i}}}$	$f_{C^C_{l_{\alpha^3_{M_i}}}}$	$f_{C_{l_p}}$	f_{L_μ}	**Fit error (Hz)**
1	1.0000	1.0000	1.0000	0.8958	1.0000	0.9838	0.0000	0.0491
2	0.9500	0.9500	1.0000	0.9400	0.9400	1.0000	0.0000	0.3308
3	1.0070	1.0000	1.0000	1.0000	1.0000	1.0000	0.0000	–0.2756
4	0.6373	0.6488	0.9971	1.0133	1.0000	1.0011	0.9328	0.2012
5	0.6373	0.6488	0.9971	1.0133	1.0000	1.0011	1.0002	0.2092

9. Validation of Coupled CFD/RBD Approach

The parameter estimation results provided an assessment of the theoretical models and input data for the aerodynamics and bearing friction. While this investigation implicitly compared the coupled CFD/RBD simulations to experiments, a more direct validation was undertaken. The conditions of the WT experiments examined in cases 4 and 5 were reproduced in the coupled CFD/RBD simulations. An exact replica of the flight control algorithms was used in the experiments and simulations. The parameter estimation was critical to this exercise since the bearing friction was represented with the model and input data for the simulations. An actuator model was also utilized in the coupled CFD/RBD simulations. The actuator response was modeled as a first order system (0.015 s time constant) with time delay (0.030 s). The interested reader can see Fresconi et al. (*8*) for more details on the actuation technology and characterization.

The deflection and roll rate from the experiment and coupled CFD/RBD simulation for case 4 are provided in figures 28 and 29. The step input responses for the deflections primarily match to within experimental scatter. The resulting roll behaviors in figure 29 demonstrate agreement to within less than 1 Hz between experiment and simulation. Fin cant causes positive roll acceleration. The parameter estimation results showed that the fin cant during WT experiments was about 36% less than the CFD/RBD simulations. This explains the consistently higher values of roll rate for the CFD/RBD results seen in figure 29. Uncertainty in the bearing friction may also factor into the differences, especially since at short times the roll rate does not hold constant at zero like the experiments indicate.

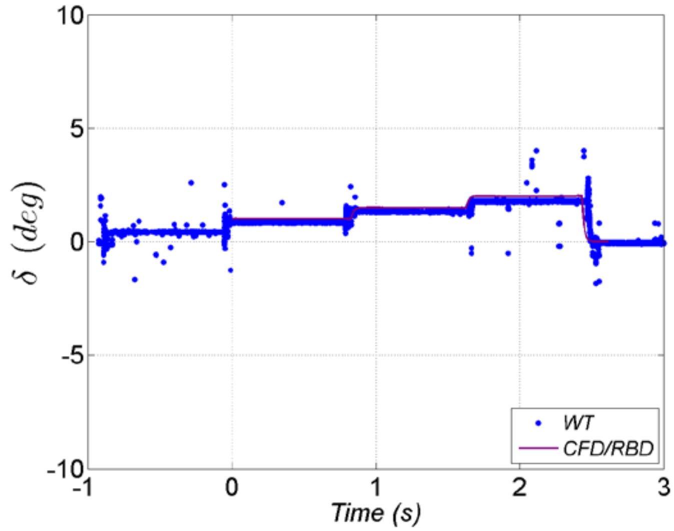

Figure 28. Experimental and coupled CFD/RBD deflection for case 4.

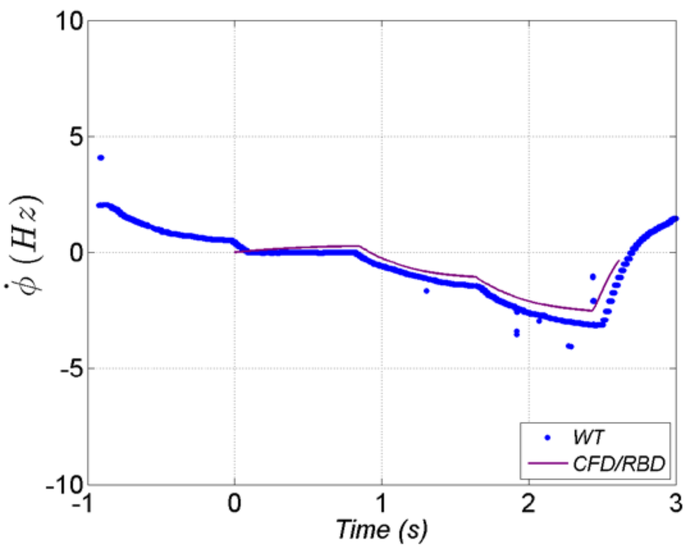

Figure 29. Experimental and coupled CFD/RBD roll rate for case 4.

Validation results for case 5 are presented in figures 30 and 31. Deflection and roll rate histories compare well except for around 0.35 s. It is possible that minor differences in the initial roll angle or roll response could result in a different deflection command. An example would be differences of +/–45° in the roll angle error when forming this signal as outlined in equation 15.

Another explanation related to roll angle could be that, while not examined in this study, the fin roll moment could be dependent on the aerodynamic roll angle. Roll rate is near zero at this time suggesting that differences in bearing friction between experiment and simulation, as discussed for validation of case 5, could skew comparisons. Differences in fin cant between experiments and simulations are less critical for case 5 since the canard moment dominates a majority of the time. An overall comparison of roll control results indicates that the simulations capture the relevant physics observed in the experiments.

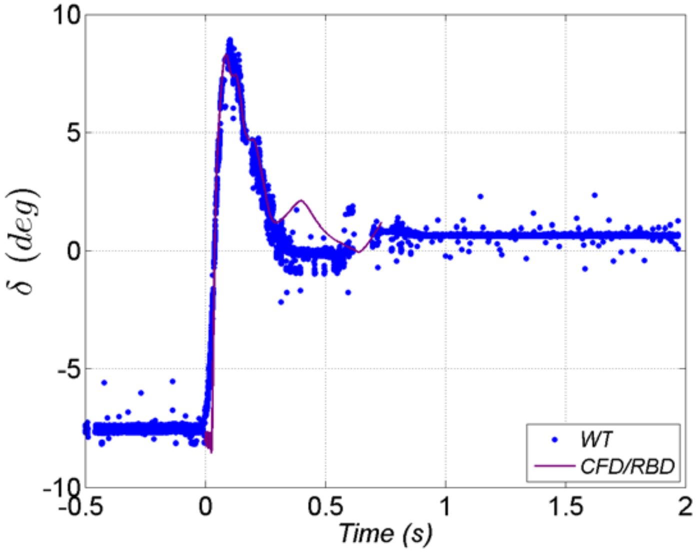

Figure 30. Experimental and coupled CFD/RBD deflection for case 5.

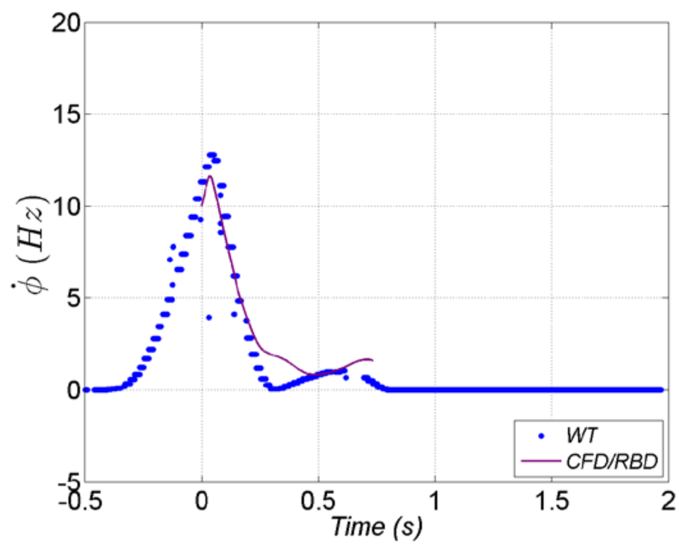

Figure 31. Experimental and coupled CFD/RBD roll rate for case 5.

10. Extended Investigation of Roll Control Using CFD/RBD Approach

These validation efforts provide confidence that coupled CFD/RBD simulations may now be extended to investigate free-flight control performance under a wider range of conditions. No bearing friction is present in these calculations for free-flight conditions. Initial roll angle, total angle of attack, and initial roll rate were varied with common gains ($K_{\phi} = 0.036$, $K_{\dot{\phi}} = 0.0055$) in the controller for all cases. A bias was applied to canard commands to counteract the roll torque due to fin cant for the purpose of reducing the steady-state roll rate to a value more suitable for free-flight. The actuator model and input data described earlier were used. The goals of this roll control exercise are to bring down the spin rate to zero and also to roll the projectile to an "X" configuration.

The results as a function of initial roll angle are given in figure 32. These simulations were conducted at an initial roll rate of 2 Hz and 5° angle of attack. The time-step used in these coupled calculations was 1.74e-04 s. Other time-steps, one twice and the other half this one, were used to determine the effect of time-step and the differences in the roll dynamics results were found to be negligible with a time-step of 1.74e-04 s or less. Each subplot shows the canard deflection, roll moment, roll rate, and roll angle. Curves on each subplot represent the different initial roll angles ($\phi_0 = 0, 22.5, 45, 67.5°$). The red dashed lines on the roll angle subplot provide the closest roll symmetry points. The time delay in the actuator model is evident for the first 0.03 s of the deflection history. Peak deflection increases with initial roll angle. The trends are similar for $\phi_0 = 0, 22.5, 45°$. The shape of the deflection history changes for $\phi_0 = 67.5°$ due to the roll angle error signal. Essentially, for times between about 0.03 and 0.06 s the closest roll symmetry point is at $\phi = 135°$ instead of $\phi = 45°$. The roll moment scales mainly with the canard deflection since roll damping and fin roll torque are relatively small for this case. There is about 1° of deflection required to counteract the fin roll torque and small total roll moment past about 0.2 s. The roll rate and roll angle responses show reasonable performance (e.g., roll angle set point tracking error less than 10° for most cases within 0.2 s). Response is least effective for $\phi_0 = 67.5°$ but this represents a more stressing condition. The initial roll angle is greater than the closest roll symmetry point so the control action must fight against the fin cant. If the initial roll angle were greater, then the controller could lock in at $\phi = 135°$. Furthermore, the sign of the terms in the controller due to the roll angle error and roll rate error are opposite so the control objectives do not align. It should be noted that more control authority is available since the peak deflection is less than only 6°. Increasing the gains further influences the robustness and may ultimately lead to instability for some conditions. More complex schemes such as scheduling roll angle gain with roll rate and adaptive control may improve performance (e.g., reducing roll angle error below a few degrees at later times as shown in bottom-right sub-plot in figure 32).

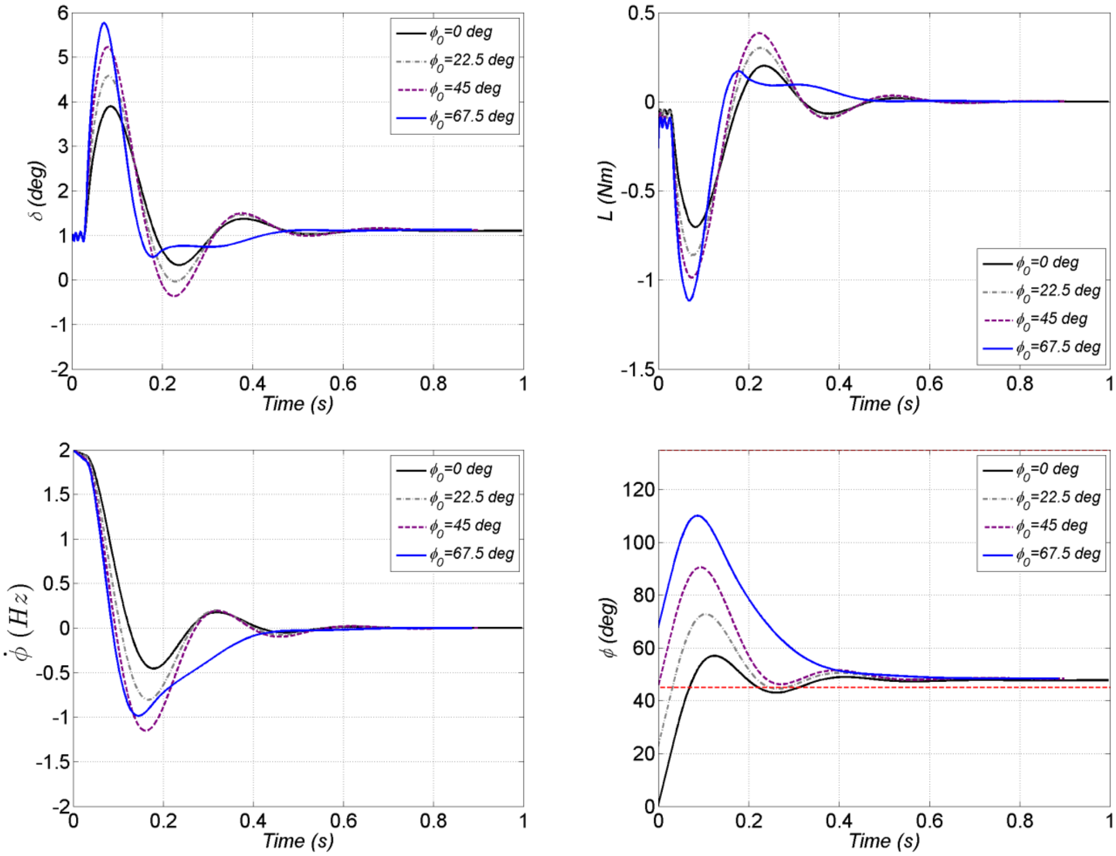

Figure 32. Coupled CFD/RBD for different initial roll angles.

Coupled CFD/RBD results are presented next for total angles-of-attack of 0° and 5° and an initial roll rate of 2 Hz and initial roll angle of 0° in figure 33. Canard deflection, roll moment, roll rate, and roll angle are similar for these two angles-of-attack. Modest control action (e.g., less than 4°) is demanded to get the roll angle error less than a few degrees within 0.2 s. These results will be strikingly different if the same gains are used with angles-of-attack yielding canard stall effects. Earlier results (e.g., figures 14 and 15) illustrated nonlinearities due to flow separation on the canards around local angle of attack of 10°. For a spinning flight body at angle of attack, the local angle of attack, and therefore aerodynamic forces and moments at each canard change rapidly. Furthermore, complex interactions between vortices shed from the canards and impinging on downstream surfaces such as fins can change the fin roll torque. This discussion simply highlights the nonlinearities associated with mechanics and control of projectiles at higher angles of attack; the results shown in figure 33 are not expected to hold at $\alpha = 10°$ or higher. Further research would be needed to address this at higher angles of attack.

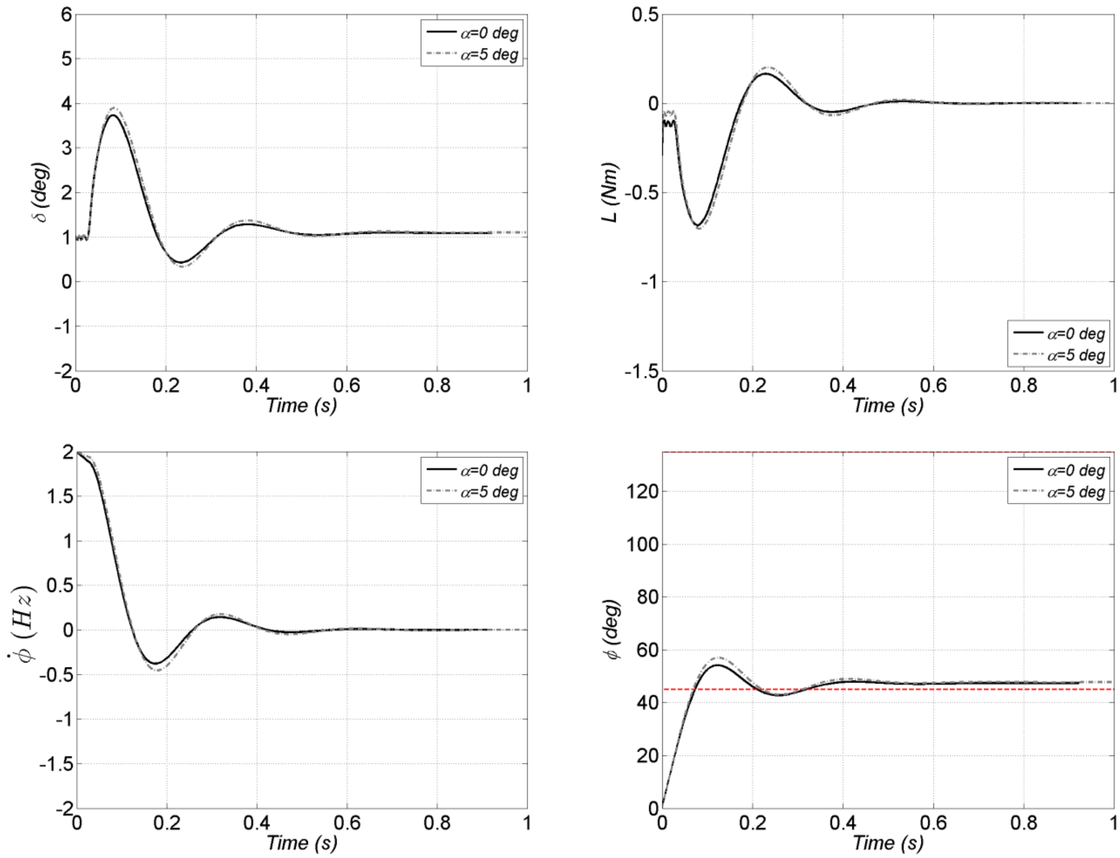

Figure 33. Coupled CFD/RBD for different total angles-of-attack.

Figure 34 demonstrates the effect of different initial roll rates at an angle of attack of 0°. Canard deflection angle increases with the increase in the initial roll rate. Saturation is barely reached for $\dot{\phi}_0 = 10$ Hz. The actuator dynamics are apparent in the deflection data for $\dot{\phi}_0 = 10$ Hz. The effect of roll damping is evident in the different values of the roll moment at time zero for $\dot{\phi}_0 = 2$ Hz and $\dot{\phi}_0 = 10$ Hz and also in the manner in which the roll moment changes even though the deflection is about constant (between times 0.08 s and 0.15 s) for $\dot{\phi}_0 = 10$ Hz. Both initial roll rate cases control the roll rate error to less than 1 Hz within about 0.2 s. The roll angle control and commands for $\dot{\phi}_0 = 10$ Hz are more complicated due to arguments concerning opposite signs in the controller terms provided for the different initial roll angle cases. Different techniques such as the adaptive control, etc., can be used to improve performance and should be investigated in the future to mitigate these behaviors. Regardless, even with $\dot{\phi}_0 = 10$ Hz the controller "catches" within one revolution (see the roll angle subplot in figure 34). Overall, the CFD/RBD approach was successfully applied to demonstrate suitable performance over a wide range of conditions using a simple controller and identify future research investigations for improving control further. These results illustrate the utility of high-fidelity modeling of the flight physics in the control formulation.

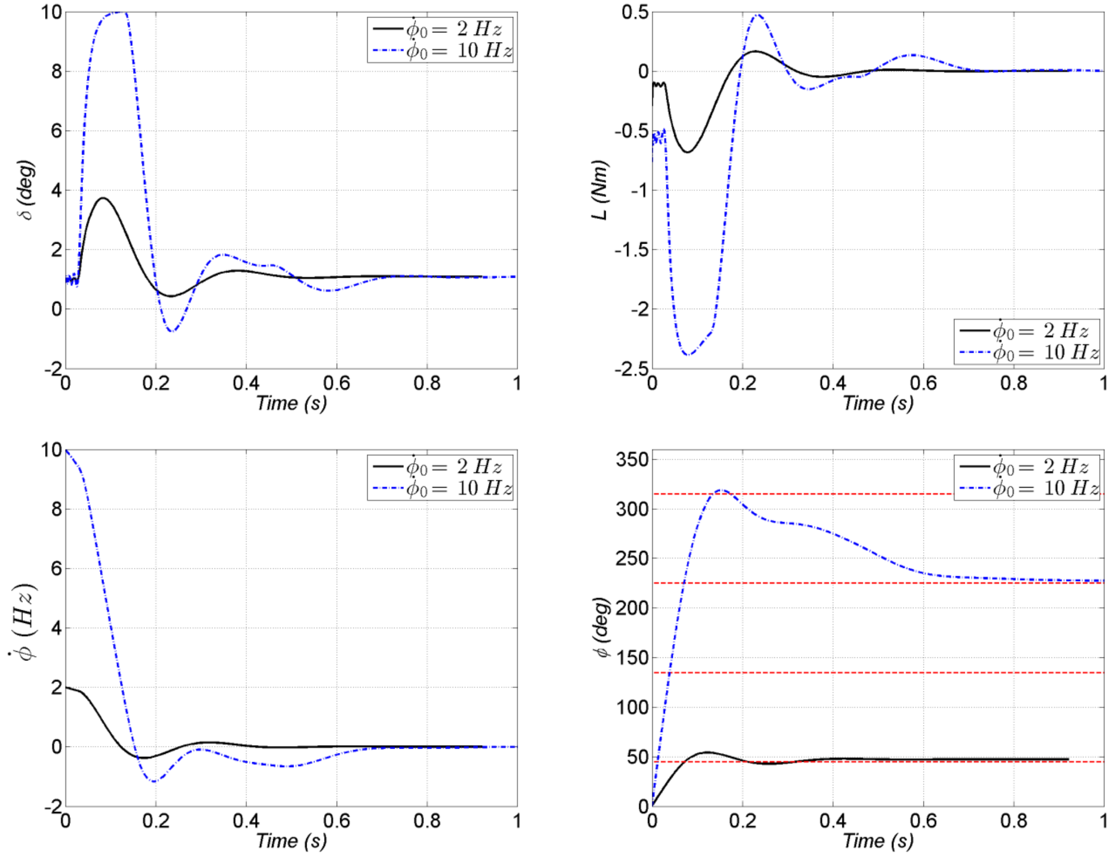

Figure 34. Coupled CFD/RBD for different initial roll rates.

11. Conclusions

This study examined the aerodynamics and flight mechanics of a canard-controlled, fin-stabilized projectile. Advanced CFD techniques were applied and simplified roll dynamics equations of motion were derived. An aerodynamic model was proposed for this configuration. Roll control algorithms were developed and implemented in coupled CFD/RBD simulations. Parameter estimation algorithms were described, which, when exercised on the results of the CFD/RBD simulations and WT experiments, showed that the aerodynamic model sufficiently characterizes flight motions for this configuration.

Comparisons between coupled CFD/RBD simulations and WT experiments were favorable. These results suggest that maneuvers in coupled CFD/RBD simulations seem to properly capture the relevant physics for canard-controlled, fin-stabilized projectiles. Roll control algorithms were designed based on the aerodynamic model and parameter estimation provided in this study. Roll control performance under a variety of conditions, assessed from simulation and experimental results, was satisfactory. Roll rate was brought to zero and roll angle regulated to the proper set-point to within reasonable errors in a sufficient time frame with modest deflection commands.

These validation efforts provided confidence, and the coupled CFD/RBD simulations were then extended to investigate free-flight roll control performance under a wider range of conditions. The effect of initial roll angle, total angle of attack, and initial roll rate on the roll control performance was investigated. Overall, the CFD/RBD approach demonstrated suitable performance over this wide range of conditions using a simple controller. The results illustrate the utility of high-fidelity modeling of the flight physics in the control formulation.

Further research investigations are required to optimize control gain parameters. More complex control schemes such as scheduling roll angle gain with roll rate and adaptive control may be needed to further improve roll control performance.

12. References

1. McCoy, R. L. *Modern Exterior Ballistics*; Schiffer Publishing Ltd.: Atlen, PA, 1999.

2. Murphy, C. H. *Free Flight Motion of Symmetric Missiles*; BRL-1216; U.S. Army Ballistics Research Laboratory: Aberdeen Proving Ground, MD, July 1963.

3. Arrow Tech Assoc. *PRODAS User Manual*; South Burlington, VT, 1997.

4. Costello, M.; Rogers, J. *BOOM: A Computer-Aided Engineering Tool for Exterior Ballistics of Smart Projectiles*; ARL-CR-670; U.S. Army Research Laboratory: Aberdeen Proving Ground, MD, June 2011.

5. Montalvo, C.; Costello, M. Effect of Canard Stall on Projectile Roll and Pitch Damping. *Journal of Aerospace Engineering* **2011,** *225*, 1003–1011.

6. Cooper, G. R.; Fresconi, F. E.; Costello, M. Flight Stability of an Asymmetric Projectile With Activating Canards. *Journal of Spacecraft and Rockets* **2012,** *49* (1), 130–135.

7. Fresconi, F. E.; Harkins, T. Experimental Flight Characterization of Asymmetric and Maneuvering Projectiles from Elevated Gun Firings. *Journal of Spacecraft and Rockets* **2012,** *49* (6), 1120–1130.

8. Fresconi, F. E.; Celmins, I.; Ilg, M.; Maley, J. Projectile Roll Dynamics and Control With a Low-Cost Skid-to-Turn Maneuver System. *Journal of Spacecraft and Rockets* **2014,** *51* (2), 624–627.

9. Moore, F. G.; Moore, L. Y. Approximate Method to Calculate Nonlinear Rolling Moment Due to Differential Fin Deflection. *Journal of Spacecraft and Rockets* **2012,** *49* (2), 250–260.

10. DeSpirito, J.; Vaughn, M. E.; Washington, W. D. Numerical Investigation of Canard-Controlled Missile with Planar and Grid Fins. *Journal of Spacecraft and Rockets* **2003,** *40* (3), 363–370.

11. Wise, K. A.; Broy, D. J. Agile Missile Dynamics and Control. *Journal of Guidance Control, and Dynamics* **1998,** *21* (3), 441–449.

12. Blair, A. B.; Dillon, J. L.; Watson, C. B. Experimental Study of Tail-Span Effects on a Canard-Controlled Missile. *Journal of Spacecraft and Rockets* **1993,** *30* (5), 635–640.

13. Pepitone, T. R.; Jacobson, I. D. Resonant Behavior of a Symmetric Missile Having Roll Orientation-Dependent Aerodynamics. *Journal of Guidance and Control* **1978,** *1* (5), 335–339.

14. Burt, J. R. *The Effectiveness of Canards for Roll Control*; TR-RD-77-8; U.S. Army Missile Command: Redstone Arsenal, AL, November 1976.

15. Sahu, J. Time-Accurate Numerical Prediction of Free-Flight Aerodynamics of a Finned Projectile. *AIAA Journal of Spacecraft and Rockets* **2008,** *45* (5), 946–954.

16. Sahu, J. Unsteady Free flight Aerodynamics of a Spinning Projectile at A High Transonic Speed. Presented at the AIAA AFM Meeting, Honolulu, HI, 18–22 August 2008.

17. Costello, M.; Sahu, J. Using Computational Fluid Dynamic/Rigid Body Dynamic Results to Generate Aerodynamic Models for Projectile Flight Simulation. *Journal of Aerospace Engineering* **2008,** *22* (G7), 1067–079.

18. Sahu, J. Computations of Unsteady Aerodynamics of a Spinning Body at Transonic Speeds. Presented at the 27th AIAA Applied Aerodynamics Conference, San Antonio, TX, 22–25 June 2009.

19. Sahu, J. Virtual Fly-Out Simulations of a Spinning Projectile from Subsonic to Supersonic Speeds. Presented at the AIAA Applied Aerodynamics Meeting, Honolulu, HI, June 2011.

20. Sahu, J. Unsteady Aerodynamic Simulations of a Canard-Controlled Projectile at Low Transonic Speeds. Presented at the AIAA Atmospheric Flight Mechanics Meeting, Portland, OR, August 2011.

21. Sahu, J.; Costello, M.; Montalvo, C. Development and Application of Multidisciplinary Computational Techniques for Projectile Aerodynamics Paper No. ICCFD7-4504; 7th International Conference on Computational Fluid Dynamics, Big Island, HI, July 2012.

22. Sahu, J.; Fresconi, F.; Heavey, K. Unsteady Aerodynamic Simulations of a Finned Projectile at a Supersonic Speed With Jet Interaction, ARL-TR-6960, U.S. Army Research Laboratory, Aberdeen Proving Ground, MD, June 2014.

23. Morrison, P. H.; Amberntson, D. S. Guidance and Control of a Cannon-Launched Guided Projectile. *Journal of Spacecraft and Rockets* **1977,** *14* (6), 328–334.

24. Rogers, J.; Costello, M. Design of a Roll-Stabilized Mortar Projectile With Reciprocating Canards. *Journal of Guidance, Control, and Dynamics* **2010,** *33* (4), 1026–1034.

25. Slegers, N. Predictive Control of a Munition Using Low-Speed Linear Theory. *Journal of Guidance, Control, and Dynamics* **2008,** *31* (3), 768–775.

26. Costello, M. Extended Range of a Gun Launched Smart Projectile Using Controllable Canards. *Shock and Vibration* **2001,** *8*, 203–213.

27. Calise, A. J.; Sharma, M.; Corban, J. E. Adaptive Autopilot Design for Guided Munitions. *Journal of Guidance, Control, and Dynamics* **2000,** *23* (5), 837–843.

28. Jitpraphai, T.; Costello, M. Dispersion Reduction of a Direct Fire Rocket Using Lateral Pulse Jets. *Journal of Spacecraft and Rockets* **2001,** *38* (6), 929–936.

29. Calise, A. J.; El-Shirbiny, H. A. An Analysis of Aerodynamic Control for Direct Fire Spinning Projectiles, AIAA Paper 2001-4217. *Proceedings of the AIAA Guidance, Navigation and Control Conference and Exhibit,* Montreal, Canada, 6–9 August 2001.

30. Burchett, B.; Costello, M. Model Predictive Lateral Pulse Jet Control of an Atmospheric Rocket. *Journal of Guidance, Control, and Dynamics* **2002,** *25* (5), 860–867.

31. Ollerenshaw, D.; Costello, M. Model Predictive Control of a Direct Fire Projectile Equipped With Canards. *Journal of Dynamic Systems, Measurement, and Control* **2008,** *130*, 061010-1–061010-11.

32. Pamadi, K. B.; Ohlmeyer, E. J.; Pepitone, T. R. Assessment of a GPS Guided Spinning Projectile Using an Accelerometer-Only IMU, AIAA Paper 2004-4881. *Proceedings of the Guidance, Navigation and Control Conference and Exhibit*, Providence, RI, 16–19 August 2004.

33. Pamadi, K. B.; Ohlmeyer, E. J.; Evaluation of Two Guidance Laws for Controlling the Impact Flight Path Angle of a Naval Gun Launched Spinning Projectile, AIAA Paper 2006-6081. *Proceedings of the Guidance, Navigation and Control Conference and Exhibit,* Keystone, CO, 21–24 August 2006.

34. Hahn, P. V.; Frederick, R. A. Slegers, N. Predictive Guidance of a Projectile for Hit-to-Kill Interception. *IEEE Transactions on Control Systems Technology* **2009,** *17* (4), 745–755.

35. Phillips, C. A. Guidance Algorithm for Range Maximization and Time-of-Flight Control of a Guided Projectile. *Journal of Guidance, Control, and Dynamics* **2008,** *31* (5), 1447–1455.

36. Chandgadkar, S.; Costello, M.; Dano, B.; Liburdy, J.; Pence, D. Performance of a Smart Direct Fire Projectile Using Ram Air Control Mechanism. *Journal of Dynamic Systems, Measurement, and Control* **2002,** *124*, 606–612.

37. Fresconi, F. E. Guidance and Control of a Projectile With Reduced Sensor and Actuator Requirements. *Journal of Guidance, Control, and Dynamics* **2011,** *34* (6), 1757–1766.

38. Theodoulis, S.; Gassmann, V.; Wernert, P.; Dritsas, L.; Kitsios, I.; Tzes, A. Guidance and Control Design for a Class of Spin-Stabilized Fin-Controlled Projectiles. *Journal of Guidance, Control, and Dynamics* **2013,** *36* (2), 517–531.

39. Nesline, F. W.; Wells, B. H.; Zarchan, P. Combined Optimal/Classic Approach to Robust Missile Autopilot Design. *Journal of Guidance, Control, and Dynamics* **1981,** *4* (3), 316–322.

40. Nesline, F. W.; Zarchan, P. Why Modern Controllers Can Go Unstable in Practice. *Journal of Guidance, Control, and Dynamics* **1984,** *7* (4), 495–500.

41. Talole, S. E.; Godbole, A. A.; Kohle, J. P.; Phadke, S. B. Robust Roll Autopilot Design for Tactical Missiles. *Journal of Guidance, Control, and Dynamics* **2011,** *34* (1), 107–117.

42. Kang, S.; Kim, H. J.; Lee, J.; Jun, B.; Tahk, M. Roll-Pitch-Yaw Integrated Robust Autopilot Design for a High Angle-of-Attack Missile. *Journal of Guidance* Control *and Dynamics* **2009,** *32* (5), 1622–1628.

43. Arrow, A.; Williams, D. E. Comparison of Classical and Modern Missile Autopilot Techniques. *Journal of Guidance* **1989,** *12* (2), 220–227.

44. Williams, D. E.; Friedland, B.; Madiwale, A. N. Modern Control Theory for Design of Autopilots for Bank-to-Turn Missiles. *Journal of Guidance* **1987,** *10* (4), 378–386.

45. Pointwise, Inc. *Gridgen Version 15 User's Manual*; Bedford, TX, 2005.

46. Steger, J.; Dougherty, C.; Benek, J. A. *Chimera Grid Scheme Advances in Grid Generation, Vol. ASME FED-Vol. 5*, American Society of Mechanical Engineers, Fairfield, NJ, 1983.

47. Peroomian, O.; Chakravarthy, S.; Goldberg, U. A. Grid-Transparent' Methodology for CFD, AIAA Paper 97-07245. *Proceedings of the 35th Aerospace Sciences Meeting and Exhibit*, Reno, NV, 6–9 January 1997; AIAA: Reston, VA, 1997.

48. Peroomian, O.; Chakravarthy, S.; Palaniswamy, S.; Goldberg, U. Convergence Acceleration for Unified-Grid Formulation Using Preconditioned Implicit Relaxation, AIAA Paper 98-0116. Presented at the 36th Aerospace Sciences Meeting and Exhibit, Reno, NV, 1998.

49. Goldberg, U. C.; Peroomian, O.; Chakravarthy, S. A. Wall-Distance-Free K-E Model With Enhanced Near-Wall Treatment. ASME Journal of Fluids Engineering, Vol. 120, pp. 457-462, 1998.

50. Franklin, G. F.; Powell, J. D.; Emami-Naeini, A. Feedback Control of Dynamic Systems, Prentice-Hall, 2006.

51. Chapman, G.; Kirk, D. A New Method for Extracting Aerodynamic Coefficients From Free-Flight Data. *AIAA Journal* **1970,** *8* (4), 753–758.

52. Whyte, R. H.; Mermagen, W. H. A Method for Obtaining Aerodynamic Coefficients From Yawsonde and Radar Data. *Journal of Spacecraft and Rockets* **1973,** *10* (6), 384–388.

53. Hathaway, W.; Whyte, R. *Aeroballistic Research Facility Free Flight Data Analysis Using the Maximum Likelihood Method*; AFATL-TR-79-98; Air Force Armament Laboratory: Eglin Air Force Base, FL, December 1979.

54. Iliff, K. Parameter Estimation for Flight Vehicles. *Journal of Guidance* **1989,** *12* (5), 609–622.

55. Klein, V.; Morelli, E. A. Aircraft System Identification, AIAA Education Series, Reston, VA, 2006.

List of Symbols, Abbreviations, and Acronyms

$\phi, \dot{\phi}, \ddot{\phi}$	roll, roll rate, roll acceleration, rad, rad/s, rad/s^2
I_X	axial moment-of-inertia, kg m^2
m	mass, kg
D	diameter, m
$S = \frac{\pi}{4} D^2$	reference area, m^2
V	velocity, m/s
M	Mach number
$\alpha, \beta, \bar{\alpha}, \phi_A$	pitch angle of attack, yaw angle of attack, total angle of attack, aerodynamic roll angle, rad
ρ	atmospheric density, kg/m^3
$\bar{q} = \frac{1}{2} \rho V^2$	dynamic pressure, Pa
x_B, y_B, z_B	body-fixed coordinate system
C_{l_p}	roll-damping moment coefficient
CP^R	radial center-of-pressure, calibers
CP^X	axial center-of-pressure, calibers
CG_N	center-of-gravity, calibers
C_l	roll moment coefficient
N	number
δ	deflection, rad
$\vec{V}_{CG/I} = [u \quad v \quad w]^T$	velocity of projectile center-of-gravity, m/s
$\vec{\omega}_{B/I} = [p \quad q \quad r]^T$	angular velocity of projectile, rad/s
$\vec{T}_{BM_i}$	transformation matrix from body frame to ith lifting surface frame
τ	time constant, s
$\vec{x}, \vec{u}, \vec{y}, \vec{e}$	state, controls, measurement, error vector

$\vec{A}, \vec{B}, \vec{F}, \vec{C}$	system dynamics, controls, forcing function, measurement matrices
J	cost function
$\vec{K}$	gain matrix
$\vec{R}, \vec{Q}$	control error and control effort matrices
$\vec{P}$	Riccati equation matrix
t	time, s
L, F	aerodynamic roll moment, friction moment, N m
$\vec{\theta}$	parameter matrix
$\mathcal{L}$	likelihood function
$\vec{\mathbb{R}}$	covariance
$\vec{\epsilon}$	error between measurement and calculation
W, F, G, H	conservative variables, inviscid flux vector, viscous flux vector, source term
V, A	cell volume, cell area
Θ	observability map
f	factor
ξ	Levenberg-Marquardt parameter
C	canard, calculated, command
F	fin
A	aerodynamic
i	i^{th} lifting surface
$0, 1, 3, 5$	zeroeth, first, third, fifth order terms
D	delay
B	bias
M	maneuver surface, measurement
μ	friction

1 (PDF)	DEFENSE TECHNICAL INFORMATION CTR DTIC OCA
2 (PDF)	DIRECTOR US ARMY RESEARCH LAB RDRL CIO LL IMAL HRA MAIL & RECORDS MGMT
1 (PDF)	GOVT PRINTG OFC A MALHOTRA
1 (PDF)	DIR USARL RDRL WML E J SAHU